Applied Catalysis B: Environment and Energy 361 (2025) 124617

Contents lists available at ScienceDirect

Applied Catalysis B: Environment and Energy

journal homepage: www.elsevier.com/locate/apcatb

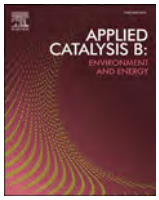

Enhanced CO_2 photoreduction in pure water systems by surface-reconstructed asymmetric Mn–Cu sites

Ganghua Zhou [a], Yun Chen [a,*], Gaoran Chen [a], Hangmin Xu [a], Weiqin Yin [a], Bin Wang [b], Xingwang Zhu [a,*], Xin Ning [a], Paul K. Chu [b,*], Xiaozhi Wang [a,c,d,**], Hui Xu [e]

[a] School of Mechanical Engineering, College of Environmental Science and Engineering, Institute of Technology for Carbon Neutralization, Yangzhou University, Yangzhou, Jiangsu 225009, PR China
[b] Department of Physics, Department of Materials Science and Engineering, and Department of Biomedical Engineering, City University of Hong Kong, Tat Chee Avenue, Kowloon, Hong Kong
[c] Joint International Research Laboratory of Agriculture and Agri-Product Safety of Ministry of Education of China, Yangzhou University, Yangzhou, Jiangsu 225009, PR China
[d] Jiangsu Collaborative Innovation Center for Solid Organic Waste Resource Utilization, Nanjing, Jiangsu 210095, PR China
[e] School of the Environment and Safety Engineering, Institute for Energy Research, Jiangsu University, Zhenjiang 212013, PR China

ARTICLE INFO

Keywords:
Photocatalysis
Cu_2O
CO_2 reduction
Syngas
Asymmetric sites

ABSTRACT

Metal-organic frameworks (MOFs) with abundant pores are excellent adsorbents for metal ions. However, the subsequent treatment of used MOFs and their reutilization still lack promising solutions. Herein, the surface-restructured Mn-doped Cu_2O (RM-Cu_2O) catalyst containing asymmetric Mn−Cu sites is prepared by glucose reduction using the spent Cu-based MOF (HKUST-1) as the precursor. The RM-Cu_2O catalyst shows good potential in tunable photocatalytic syngas (CO and H_2) production in a pure water system. The syngas ratios can be tuned from ~1:2 to ~1:1 by increasing CO production. DFT calculations and photoelectrochemical tests confirm that the asymmetric Mn−Cu sites on the RM-Cu_2O catalyst accelerate the photogenerated charge transport and optimize CO_2 adsorption and activation. *In situ* irradiation X-ray photoelectron spectroscopy is conducted to investigate the dynamic charge transport and reactions on the RM-Cu_2O catalyst. Based on *in situ* Fourier transform infrared spectroscopy and simulations, the mechanism of photocatalytic syngas production is elucidated. This work provides a promising solution for the resource utilization of the spent MOFs-based adsorbents and photocatalytic energy development.

1. Introduction

Syngas containing mainly CO and H_2 is considered a crucial product in the chemical industry as it can be used as a building block for the synthesis of value-adding fuels/chemicals such as methanol, methane, and ethylene [1,2]. Solar-driven carbon dioxide (CO_2) conversion into syngas is a promising technique that can mitigate the greenhouse effect and simultaneously develop renewable energy [3,4]. The optimized photocatalysts can induce the generation, separation, and migration of photogenerated carriers under mild reaction conditions (illumination, room temperature, and ambient pressure) to further achieve photocatalytic syngas production [5]. The overall efficiency of photocatalysis is the cumulative efficiency of the three key steps of light absorption, charge separation and transfer, as well as surface reaction [4]. The mismatch in the time scale of the above three steps results in a weak photocatalytic CO_2 reduction reaction (PCRR) activity [5]. Although extensive efforts such as phase engineering [6], external-field assistance [7], and surface engineering [8], have been made to overcome the bottlenecks limiting PCRR, PCRR systems still rely on the use of photosensitizers, sacrificial reagents, and high-concentration CO_2. However, performing PCRR in a system with pure water and CO_2 for the preparation of syngas has not been studied extensively, but it is necessary to develop photocatalysts with the potential to enhance PCRR in pure water systems for syngas production.

* Corresponding authors.
** Corresponding author at: School of Mechanical Engineering, College of Environmental Science and Engineering, Institute of Technology for Carbon Neutralization, Yangzhou University, Yangzhou, Jiangsu 225009, PR China.
E-mail addresses: cy@zxw.ac.cn (Y. Chen), zxw@yzu.edu.cn (X. Zhu), paul.chu@cityu.edu.hk (P.K. Chu), xzwang@yzu.edu.cn (X. Wang).

https://doi.org/10.1016/j.apcatb.2024.124617
Received 4 July 2024; Received in revised form 2 September 2024; Accepted 16 September 2024
Available online 17 September 2024

Cuprous oxide (Cu_2O), as an earth-abundant metal oxide, is widely employed in PCRR due to its low cost, high thermal conductivity, and suitable bandgap (~2.0 – 2.2 eV) [9]. However, it is challenging to overcome the bottleneck related to the corrosion of intrinsic Cu_2O during the redox reaction under light illumination [10]. Constructing asymmetric active centers by introducing metal dopants can modulate the local electronic structure and enhance the stability of metal compounds [11]. The affinity of the asymmetric bimetallic active centers to O and H atoms on the catalyst surface can induce the generation of various reaction intermediates and change the reaction pathway and product selectivity [12]. Recent research results demonstrate that introducing metal dopants can indeed optimize the electronic structure of the catalyst by regulating the d-band center of the metallic compound, thereby improving the adsorption and activation of the active sites and reaction intermediates [13]. The upshifted d-band center tends to increase the energy of d-orbital electrons and the bonding ability of key intermediates in PCRR (*CO_2, *COOH, *CO, etc.), giving rise to enhanced PCRR performance [13,14]. For example, Liu et al. have employed an ion exchange strategy to introduce Cd to the surface of $(CuGa)_xZn_{1-2x}Ga_2S_4$ to promote the upward movement of the d-band center [15]. The up-shifted d-band center increases the antibonding state energy, lowers the adsorption energy barrier of the PCRR intermediate, and improves the reaction activity [15]. Qian et al. have synthesized Ni-doped Co_3O_4 with Ni-Co dual sites (Ni-Co_3O_4) by *in situ* phase transformation [16]. A more negative average spin down the d-band center can lower the energy levels of the bonding and antibonding states of d_{xz}/d_{yz}-2π*, consequently weakening the bonding of *CO on Ni-Co_3O_4 as more electrons occupy the anti-bonding state [16]. Among the different transition metals, manganese (Mn) has been widely studied due to its abundance and lower cost [17]. Furthermore, Mn is a relatively active transition metal because of the empty and occupied orbitals [18]. Low-valent Mn cations may provide more unpaired d electrons for higher surface reactivity than high-valent metal cations [19]. Hence, Mn incorporation into metal compounds can optimize the formation of intermediates in the CO_2 reduction reaction and reduce the activation energy barrier for CO_2 [20]. Inspired by previous works, we speculate that the interaction between the key reaction intermediates and the catalyst surface can be optimized by constructing asymmetric bimetallic active centers in Cu_2O to enhance PCRR performance.

In this work, simple glucose reduction is used to synthesize surface-reconstructed Mn-doped Cu_2O (RM-Cu_2O) in one step using Mn pre-saturated Cu-based MOF (HKUST-1) as the precursor. Density-functional theory (DFT) calculations show that the Mn dopants upshift the d-band center of RM-Cu_2O, resulting in energy accumulation at the Mn sites. The RM-Cu_2O catalyst with asymmetric Mn−Cu sites shows excellent photocatalytic CO_2 conversion into syngas. *In situ* irradiation X-ray photoelectron spectroscopy is employed to study the dynamic changes of the metal valence states on the catalyst. *In situ* Fourier transform infrared spectroscopy (*in situ* FTIR) is performed together with DFT calculations to show that the asymmetric Mn−Cu sites activate CO_2 molecules and reduce the formation energy barrier of the important reaction intermediate *COOH in PCRR. The results reveal a feasible strategy for the synthesis, electronic structure control, and secondary utilization of MOF-based adsorbent-derived doped metal oxides.

2. Experimental section

2.1. Materials

Copper (II) nitrate hydrate ($Cu(NO_3)_2{\cdot}3H_2O$, AR), ethanol (absolute, AR), manganese (II) chloride tetrahydrate ($MnCl_2{\cdot}4H_2O$, AR), sodium hydroxide (NaOH, AR), and glucose ($C_6H_{12}O_6$, AR) were purchased from Sinopharm Chemical Reagent Co., Ltd. 1,3,5-Benzenetricarboxylic acid (H_3BTC, 98 %) and polyvinylpyrrolidone (K30, M.W. ~40,000) were acquired from Aladdin Industrial Corp. All the chemicals were used without further purification.

2.2. Synthesis of HKUST-1 and Mn-HKUST-1

HKUST-1 was synthesized with minor modifications based on previous literature [21]. $Cu(NO_3)_2{\cdot}3H_2O$ (3.6 mmol) was dissolved in 15 mL of deionized water to obtain solution A, and H_3BTC (2 mmol) was dissolved in 15 mL of absolute ethanol containing 0.2 g of PVP to obtain solution B. Solution A was mixed with solution B, stirred for 1 h, transferred to a 50 mL polytetrafluoroethylene-lined stainless-steel reactor, and reacted hydrothermally at 120 °C for 10 h. After natural cooling to room temperature, the blue powder sample was rinsed several times with deionized water and absolute ethanol and vacuum dried at 60 °C overnight to produce HKUST-1.

Further, 1 g of HKUST-1 was added to 200 mL of a 50 g/L Mn ion solution and stirred for 5 h until adsorption was saturated. It was filtered and vacuum-dried to produce the Mn-HKUST-1 precursor.

2.3. Synthesis of surface-reconstructed Mn-doped Cu_2O (RM-Cu_2O)

The Mn-HKUST-1 precursor (0.3 g) was added to 40 mL of deionized water and dispersed ultrasonically. The 0.8 M NaOH solution (10 mL) was added dropwise to the above solution and stirred in an 80 °C water bath for 5 min. After that, 3.42 g of glucose was added to the mixture. The reaction proceeded in the 80 °C water bath for 1 hour. Finally, the sample was filtered, washed with deionized water and ethanol, and vacuum-dried to obtain a targeted RM-Cu_2O catalyst.

2.4. Photocatalytic experiment

The photocatalytic CO_2 reduction test was performed in an online system (μGAS, Beijing Perfectlight, China). The sample (5 mg) was dispersed ultrasonically in 5 mL of deionized water. After evacuation for 30 min to remove air, high-purity CO_2 (>99.999 %) was introduced into the reaction system to a pressure of 80 kPa. The temperature was kept at 283.15 K by circulating cooling water. The light source was a 300 W Xenon lamp (Beijing Perfectlight, PLS-SXE300+/UV, wavelength 300–2500 nm, light intensity 100 mW/cm^2). The gas products were determined on a gas chromatograph (FULI GC9790II, Ar carrier) equipped with a hydrogen flame ionization detector (FID) and thermal conductivity detector (TCD).

Consistent with the conditions of the PCRR experiments, control tests without light, without photocatalysts, and with argon (Ar) instead of CO_2 were performed. The same reaction conditions were adopted in the ^{13}C isotope tracing tests, but $^{13}CO_2$ was employed instead of $^{12}CO_2$. The collected gas products were analyzed by gas chromatography/mass spectrometry.

3. Results and discussion

Density-functional theory calculations are first conducted to evaluate the potential effects of Mn doping of RM-Cu_2O on the electronic structure and surface adsorption properties. As shown in Fig. 1a, the PDOS results show that RM-Cu_2O with an asymmetric Mn−Cu site has a narrower band gap than pristine Cu_2O because of the acceptor impurity energy levels and strong hybridization of Cu 3*d* and O 2*p* orbitals [22]. More energy levels in RM-Cu_2O cross the Fermi level compared to pristine Cu_2O, indicating higher conductivity [23]. The representative 3*d* electrons of Cu atoms in Cu_2O are at −1.72 and −1.52 eV below the Fermi level, while they shift to −1.62 and −1.42 eV in RM-Cu_2O, suggesting that the asymmetric Mn−Cu sites in RM-Cu_2O endow Cu atoms with a larger electron density enabling Cu 3*d* to be closer to the Fermi level for better photocatalytic CO_2 reduction reaction (PCRR) activity [24]. In particular, the unoccupied antibonding orbitals of Cu atoms shift below the Fermi level. Therefore, the number of empty orbitals that can be occupied by electrons of Cu 3*d* increases to give rise to a stronger CO_2 activation capacity [25]. The d-band center and CO_2 adsorption energy are calculated, and as expected, RM-Cu_2O with asymmetric

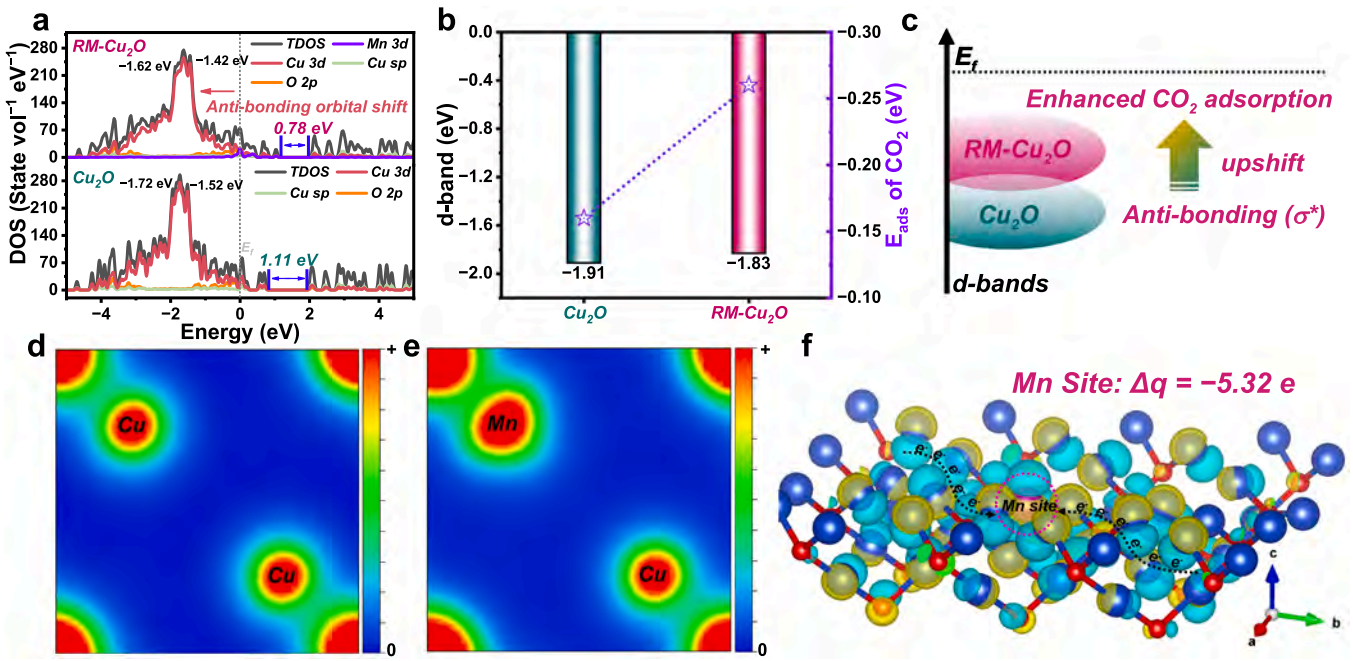

Fig. 1. Theoretical studies: (a) PDOS plots of Cu, O, and Mn atoms in the catalysts; (b) Relationship between the d-band center and CO_2 adsorption energy on Cu_2O and RM-Cu_2O; (c) Schematic diagram showing the orbital interactions between the photocatalyst and adsorbate; Charge density distributions of (d) Cu_2O and (e) RM-Cu_2O; (f) Charge density difference at the Mn site.

Mn−Cu sites shows an improved d-band center relative to the Fermi level compared to pristine Cu_2O (Fig. 1b). This upwardly shifted d-band center (near the Fermi level) further enhances the CO_2 adsorption and activation by increasing the antibonding state energy and improves the conversion efficiency of PCRR [14,26]. The CO_2 adsorption energy is also derived, and that on RM-Cu_2O is significantly stronger than that on Cu_2O. Hence, regulating the d-band center by constructing asymmetric Mn−Cu sites can optimize the adsorption of CO_2 to reduce the energy barrier of PCRR (Fig. 1c).

To understand how the reconstructed asymmetric Mn−Cu sites regulate the CO_2 activation process, the charge density distribution is calculated. As shown in Figs. 1d and e, the charge density at Mn sites on RM-Cu_2O has a bigger charge density than the pristine Cu_2O, implying that the constructed asymmetric Mn−Cu sites may serve as the active center to regulate and optimize the electronic structure [27]. For confirmation, the differential charge density of the Mn site is derived. As shown in Fig. 1f, more electrons gather at the Mn site. The Bader charge analysis discloses that the Mn site gains nearly 5.32 electrons from surrounding atoms, thus corroborating that it is an effective electron capture/transfer center [28]. All in all, the results indicate that surface reconstruction by Mn doping improves the electronic structure of Cu_2O and PCRR.

Cu_2O and reconstructed Mn-doped Cu_2O (RM-Cu_2O) are synthesized from the Cu-based MOF (HKUST-1) by a simple glucose reduction method as illustrated in Fig. 2a and Fig. S1. The powder X-ray diffraction (XRD) patterns (Fig. S2) confirm the successful preparation of HKUST-1. The structure of Mn-HKUST-1 changes after Mn doping. After pre-saturation of Mn^{2+} adsorption by HKUST-1, the morphology of HKUST-1 changes from an octahedron (Fig. S3) to a long strip (Fig. S4). The scanning electron microscopy (SEM) image of the undoped Cu_2O (Fig. 2b) exhibits a cubic morphology with predominantly a micrometer size, while the surface-reconstructed RM-Cu_2O (Fig. 2c) shows a sphere-like morphology tens of nm to 300 nm in size. The transmission electron microscopy (TEM) image (Fig. 2d) verifies the above observation. The reduced particle size can be attributed to the dilution effect because of Mn doping. The high-resolution TEM (HR-TEM) image (Fig. 2e) reveals lattice spacings of 3.01, 2.13, 2.46, and 1.74 Å corresponding to the (110), (200), (211), and (111) planes of Cu_2O. Energy-dispersive X-ray spectroscopy (EDX) (Fig. S5) confirms the presence of Cu, O, and Mn in RM-Cu_2O. The high-angle annular dark-field scanning TEM (HAADF-STEM) images (Fig. 2f) and EDS maps (Fig. 2g) reveal that Mn, Cu, and O are distributed uniformly and Mn is dispersed on the surface of Cu_2O due to the different redox potentials between Mn and Cu during glucose reduction. Aberration-corrected STEM (AC-STEM) is employed to investigate the Mn site, and no obvious metallic Mn or MnO_x nanoparticles are observed (Fig. S6). Since the atomic number of Mn is smaller than that of Cu, it is difficult to directly observe the atomic image of Mn. Nonetheless, based on selected-area AC-STEM results of RM-Cu_2O (Figs. 2h–j), Cu and Mn co-exist in the RM-Cu_2O crystal lattice. The results verify the synthesis of RM-Cu_2O with asymmetric Mn−Cu sites.

The powder X-ray diffraction (XRD) pattern (Fig. S7a) demonstrates the high purity of cubic phase Cu_2O with a space group of Pn-3m (224) (PDF#77–0199). No obvious peaks related to metallic Mn or MnO_x are detected because Mn is incorporated uniformly into the Cu_2O lattice during surface reconstruction. The peak of the dominant (111) plane of RM-Cu_2O shows a positive shift close to 0.1° maybe due to the lattice stretching of Cu_2O caused by Mn. Fourier transform infrared spectroscopy (FTIR) is performed to analyze the chemical bonds and surface functional groups. As shown in Fig. S7b, the peak at 632.9 cm^{-1} attributed to Cu−O is observed from Cu_2O [29]. The bands at 1067.1, 1116.8, and 1390.2 cm^{-1} are associated with −OH (Cu−OH) on the surface of Cu_2O [30,31]. The peak near 1630 cm^{-1} arises from the bending of the H-O-H plane of H_2O, and the broad band at 3410 cm^{-1} is from the stretching of hydrogen-bonded −OH groups from adsorbed water. After the construction of asymmetric Mn−Cu sites, a stretching peak (607 cm^{-1}) for Mn−O is observed from RM-Cu_2O [32]. There are more peaks related to Mn−O (458.4, 475.6, and 673.2 cm^{-1}) from RM-Cu_2O in the enlarged spectrum [32–34], and the peak at 1208.1 cm^{-1} stems from Mn−OH in RM-Cu_2O. These results confirm that Mn doping is successful. The peak attributable to hydroxyl groups (−OH) at 3410 cm^{-1} in RM-Cu_2O increases significantly compared to the pristine Cu_2O, meaning that RM-Cu_2O has more abundant −OH species [35]. The hydroxyl species serve as Lewis base sites to interact

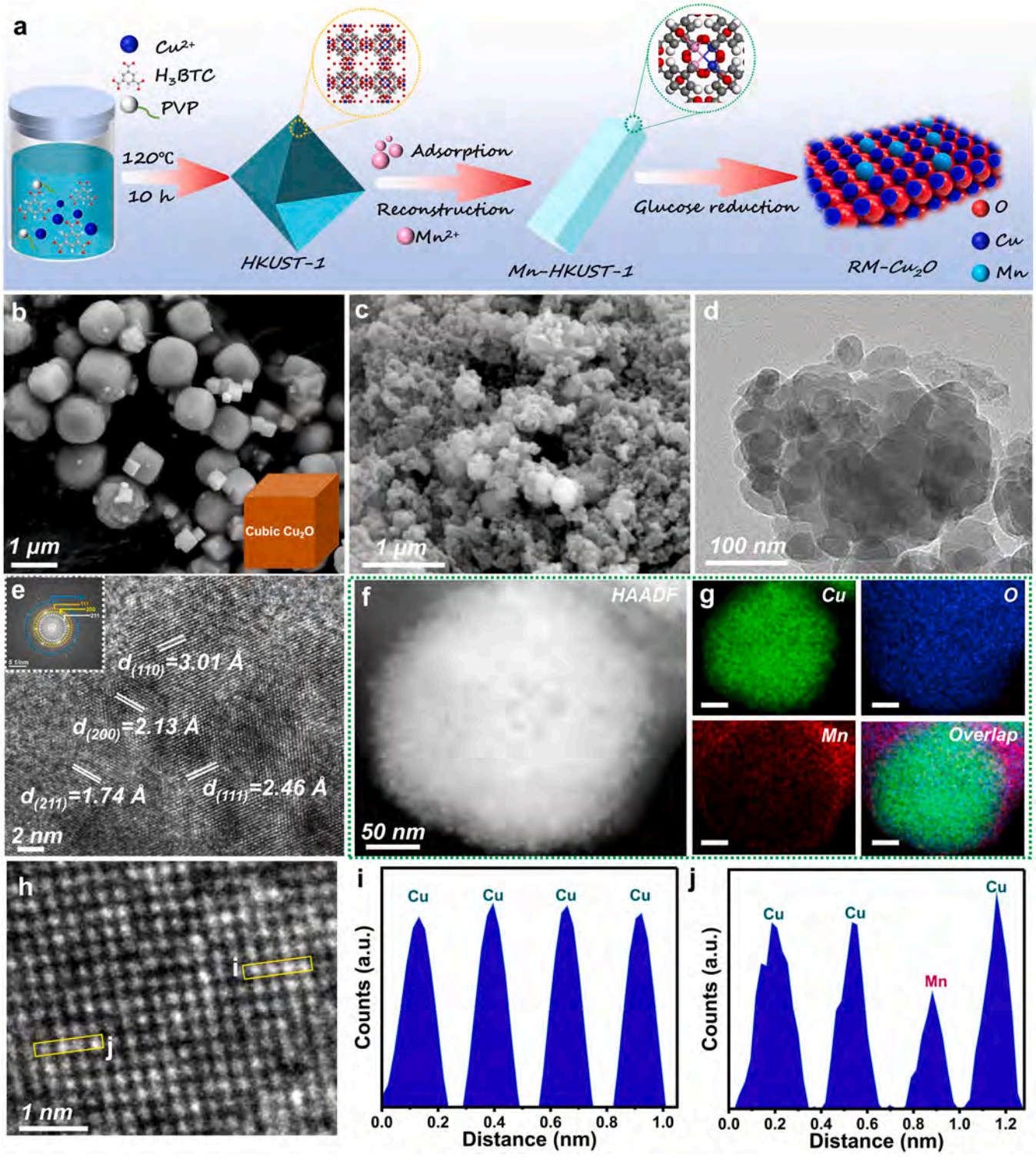

Fig. 2. Synthesis, morphology, and structure: (a) Schematic illustration of RM-Cu_2O; SEM images of (b) Cu_2O and (c) RM-Cu_2O; (d, e) HR-TEM images (inset: FFT image of the selected area); (f) HAADF-STEM image; (g) EDX elemental maps of RM-Cu_2O, scale bar: 50 nm; Line scans of Cu and Mn in the (h) selected area of (i) Cu_2O and (j) RM-Cu_2O.

with Lewis acid sites (metal ions) to form frustrated Lewis acid-base pairs, which accelerate CO_2 activation and enhance PCRR [36].

Fig. S8 shows the presence of Cu, O, and Mn in RM-Cu_2O. The high-resolution Cu 2*p* spectra (Fig. S7c) show the dominant peaks of Cu $2p_{1/2}$ at 952.4 eV and Cu $2p_{3/2}$ at 932.7 eV from Cu^+ in Cu_2O [37]. The Cu 2*p* spectrum of RM-Cu_2O shows a negative shift due to the changing electronic structure of Cu_2O after the construction of asymmetric Mn−Cu sites [38]. The Mn 2*p* spectrum (Fig. S7d) reveals Mn^{2+} in RM-Cu_2O. The Auger spectrum of Cu (Cu LMM) (Figs. S7e and f) further confirms that the valence state of Cu in Cu_2O and RM-Cu_2O is +1 without obvious metallic or oxidized states [39]. The O 1 *s* spectrum (Fig. S7g) can be deconvolved into three peaks at 530.7, 531.8, and 533.2 eV corresponding to Cu−O (lattice oxygen), surface adsorbed −OH, and H_2O, respectively [40]. After constructing asymmetric Mn−Cu sites, the

proportion of surface-adsorbed -OH increases from 25.23 % to 51.86 % consistent with FTIR analysis. The results confirm the production of reconstructed RM-Cu_2O with asymmetric Mn−Cu sites.

The UV–vis–NIR diffuse reflectance spectra (UV–vis–NIR DRS) are displayed in Fig. S9a. Both Cu_2O and RM-Cu_2O show a wide photoresponse range (200–1500 nm), and RM-Cu_2O exhibits a higher light absorption intensity than the pristine Cu_2O because the Mn dopants act as visible-light absorption centers to enhance light harvesting [22]. The results are in good agreement with the color change of RM-Cu_2O from brick red to orange-yellow after the construction of asymmetric Mn−Cu sites (inset in Fig. S9a). The bandgaps are evaluated from the Tauc plots based on the Kubelka-Munk function (Fig. S9b) [41]. The bandgaps of Cu_2O and RM-Cu_2O are approximately 2.16 and 1.82 eV, respectively. The enhanced infrared light response is believed to arise from the potential *d-d* transition and cascade electron transfer. That is, electrons in the valence band first transition to the split empty *d* orbital and then to the conduction band [42]. Ultraviolet photoelectron spectroscopy (UPS) and XPS valence band (XPS-VB) spectra are acquired to study the energy level alignment. The cutoff edges (E_C) of Cu_2O and RM-Cu_2O are determined to be 17.44 and 17.52 eV, respectively (Fig. S9c and d). The work functions (Φ) of Cu_2O and RM-Cu_2O catalysts are derived by the equation $\Phi = h\nu - E_C$, where $h\nu$ is the kinetic energy of 21.22 eV [43]. The work functions (Φ) of Cu_2O and RM-Cu_2O are calculated to be 3.78 and 3.70 eV, respectively. The Φ values of Cu_2O and RM-Cu_2O obtained by theoretical calculations (Fig. S10) show a similar trend as the experimentally determined work functions. Meantime, the valence band potential (E_{VB}) of Cu_2O and RM-Cu_2O are determined to be 1.73 and 1.69 eV (versus the Femi level) separately according to the XPS-VB spectra (Fig. S9e). The E_{VB} values of Cu_2O and RM-Cu_2O are 5.51 and 5.39 eV (versus the vacuum level) based on the formula E_{VB} (versus vacuum level) = Φ + E_{VB} (vs Femi level) [23]. The E_{VB} values of Cu_2O and RM-Cu_2O are 1.07 and 0.95 V (versus NHE), respectively, based on a conversion of −4.44 eV. Correspondingly, the conduction band potentials (E_{CB}, versus the vacuum level) of Cu_2O and RM-Cu_2O are estimated to be −1.09 and −0.87 eV, respectively. The 0.22 eV downshift of the CB stems from the acceptor impurity level formed under the CB [22]. Fig. S9f shows the band alignment, and all the catalysts meet the thermodynamic requirements for CO_2-to-CO conversion. The above results indicate that the asymmetric Mn−Cu sites expand the light absorption of Cu_2O and may promote charge separation by introducing impurity energy levels for better PCRR characteristics.

The PCRR activity is evaluated with the photocatalyst in a pure-water system by using water as the electron donor and reductant (details in the Supplementary Information). Fig. 3a shows the time-dependent conversion yields of Cu_2O and RM-Cu_2O under full-spectrum irradiation. The PCRR products of the Cu_2O catalyst are CO, methane (CH_4), ethylene (C_2H_4), and H_2 in line with the literature [44, 45]. RM-Cu_2O has superior photocatalytic activity compared to the pristine Cu_2O, yielding approximately 60.56 μmol g^{-1} of CO and 79.40 μmol g^{-1} after irradiation for 6 h. Notably, only trace amounts of CH_4 are detected, and no C_2H_4 is formed, improving the syngas purity. The CO and CH_4 generation rates from RM-Cu_2O are 2.0 and 2.6 times higher than those from pure Cu_2O, respectively (Fig. 3b). Compared with the pure Cu_2O, the ratio of CO and H_2 for RM-Cu_2O changes from approximately 1:2 to 1:1 may be due to the higher reactant (CO_2 and e^-) concentration in PCRR ($CO_2+2H^++2e^-\rightarrow CO+H_2$) with asymmetric Mn−Cu sites. As a result, the forward reaction is promoted, and the CO yield increases [46]. The O_2 yields (Fig. S11) from Cu_2O and RM-Cu_2O in overall PCRR are 0.56 and 0.98 μmol g^{-1} h^{-1}, respectively. However, the molar ratio of H_2/O_2 is not the ideal 2:1, perhaps due to the consumption of O_2 generated by the reduction of photogenerated electrons to generate superoxide radical active species. The typical signal attributable to superoxide radicals is observed by EPR (Fig. S12), which further verifies the above speculation. RM-Cu_2O also shows superior photocatalytic durability for 24 h (Fig. 3c). The evolution rates of CO and H_2 are stable, and the ratio of CO and H_2 is maintained at about 1:1 based on four continuous runs. XRD (Fig. S13) and FTIR (Fig. S14) show that the crystalline structure is preserved after PCRR, and no obvious

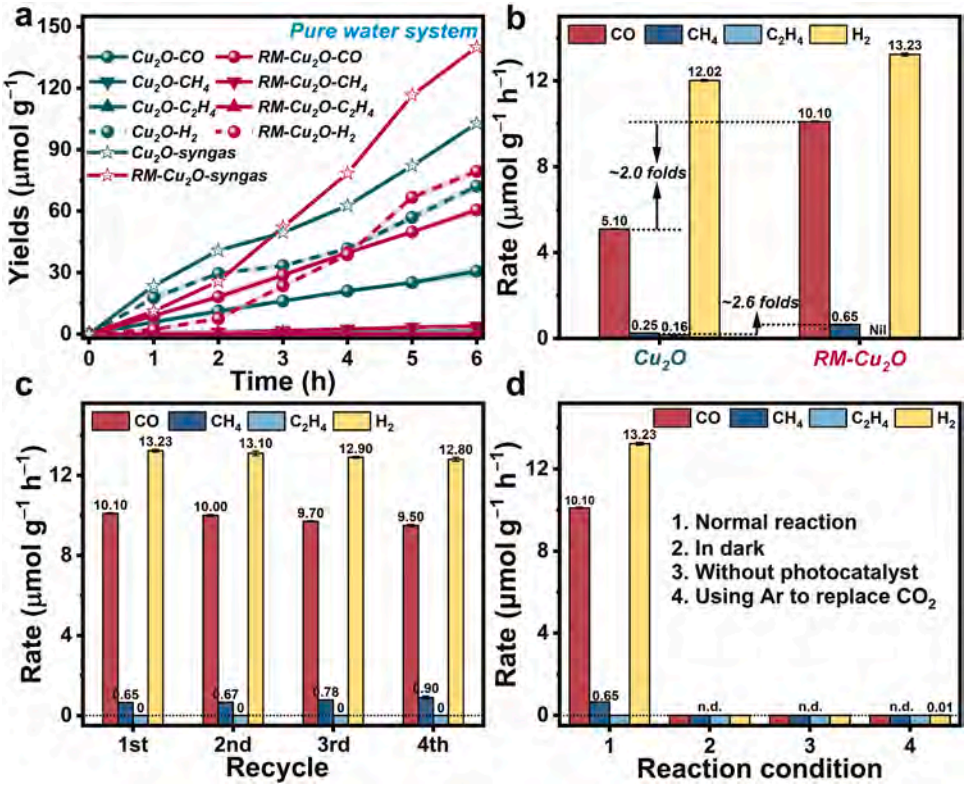

Fig. 3. Photocatalytic CO_2 conversion into syngas in a pure-water system: (a) Time-changing of products in PCRR of Cu_2O and RM-Cu_2O; (b) Evolution rates of various gas products in PCRR; (c) Durability; (d) Control experiments of RM-Cu_2O under different conditions.

agglomeration of RM-Cu_2O is observed after the reaction according to SEM (Fig. S15). Hence, RM-Cu_2O has excellent stability. Furthermore, control experiments are performed to determine the role of various components in the PCRR. As shown in Fig. 3d, no carbon-containing products are detected under the conditions of dark, catalyst-free, and Ar gas instead of CO_2. Only trace amounts of hydrogen are detected by introducing argon instead of CO_2. These results indicate that light, catalyst, and CO_2 are necessary to achieve efficient photocatalytic CO_2 conversion. Isotopic experiments (Fig. S16) are conducted to unravel the origin of CO generated by CO_2RR. Under the atmosphere of $^{13}CO_2$, the peak with a retention time of 4.83 min and dominant peak at $m/z = 29$ attributed to ^{13}CO are detected by gas chromatography/mass spectrometry (GC/MS), providing evidence that CO is converted from CO_2 during CO_2RR [47].

A series of photoelectrochemical measurements, including electrochemical impedance spectroscopy (EIS), transient photocurrent response test, steady-state photoluminescence (PL), time-resolved photoluminescence (TR-PL), surface photo-voltage (SPV), and incident photon-to-current efficiency (IPCE) measurements are performed to study the charge separation kinetics. The Nyquist plots obtained by EIS (Fig. 4a) show that RM-Cu_2O exhibits a smaller arc radius than Cu_2O, implying that the charge transfer resistance of RM-Cu_2O is less than that of Cu_2O and the photogenerated electrons in RM-Cu_2O lead to a rapid interfacial charge transfer [48]. Fig. 4b exhibits the transient photocurrent response of Cu_2O and RM-Cu_2O. RM-Cu_2O displays a remarkably improved photocurrent density compared to the pristine Cu_2O, indicative of faster charge separation [49]. The above result shows good agreement with EIS tests. Furthermore, the dynamic transfer of charge carriers is investigated by SPV measurements. As shown in Fig. 4c, RM-Cu_2O shows stronger SPV signals in the range of 300–550 nm than the pristine Cu_2O, which is consistent with its smallest arc radius in EIS (Fig. 4a) and strongest transient photocurrent response (Fig. 4b). This suggests that the asymmetric Mn−Cu site acts as an electron capturing center to inhibit the recombination of photogenerated carriers and enhance the PCRR activity [50]. Steady-state PL is carried out to investigate the migration of photogenerated charge carriers. As shown in Fig. 4d, RM-Cu_2O shows a weaker emission intensity than pure Cu_2O, suggesting a reduced recombination rate of e^--h^+ pairs [51]. Time-resolved PL spectra are acquired to calculate the average lifetime (A_τ), and as shown in Fig. 4e and Table S1, RM-Cu_2O (A_τ=1.57 ns) shows a shorter average lifetime than the pristine Cu_2O (A_τ=3.91 ns). The photogenerated carriers in RM-Cu_2O can be separated/transferred quickly, thereby actively engaging in PCRR in lieu of recombination [13]. IPCE (Fig. 4f) is determined to study the transfer efficiency of photogenerated electrons. Different wavelengths from 300 to 600 nm are selected for the photoelectrochemical tests and calculation of the IPCE values. The results show good agreement with the DRS spectra (Fig. S9a). The IPCE curve of RM-Cu_2O shows a similar light absorption tendency compared with Cu_2O, indicating that Cu_2O dominates photovoltaic conversion [52]. Light absorption gradually weakens as the wavelength increases, resulting in decreased photo-electron conversion efficiency. The IPCE values of Cu_2O and RM-Cu_2O decrease gradually with increasing wavelength. Compared to the pristine Cu_2O, the IPCE values of RM-Cu_2O improve on account of more efficient separation/-transfer in RM-Cu_2O [53]. Based on the above photoelectrochemical analysis, the RM-Cu_2O catalyst with asymmetric Mn−Cu sites shows excellent charge transport kinetics, which will facilitate more photogenerated charges to participate in PCRR.

The N_2 adsorption-desorption isotherms are measured to investigate the pore structure. As shown in Fig. S17a, both Cu_2O and RM-Cu_2O show the typical type IV isotherms with H3 hysteresis loops, implying the presence of mesopores. The Brunauer-Emmett-Teller (BET) surface area (S_{BET}) of RM-Cu_2O is 25.68 m^2/g, which is 8.42 times bigger than that of the pristine Cu_2O (3.05 m^2/g) because Mn reduces the size of the catalyst. The larger S_{BET} results in more active sites for CO_2 adsorption. The pore size distributions (Figs. S17b and c) are derived by the BJH method. RM-Cu_2O shows a smaller average diameter (5.5 nm) than Cu_2O (48.5 nm). The CO_2 adsorption capacity is determined, and interestingly, the CO_2 uptake (Fig. 5a) of RM-Cu_2O is 33.19 cm^3/g at 1 atm and 283.15 K, which is more than 1.47 times higher compared to Cu_2O

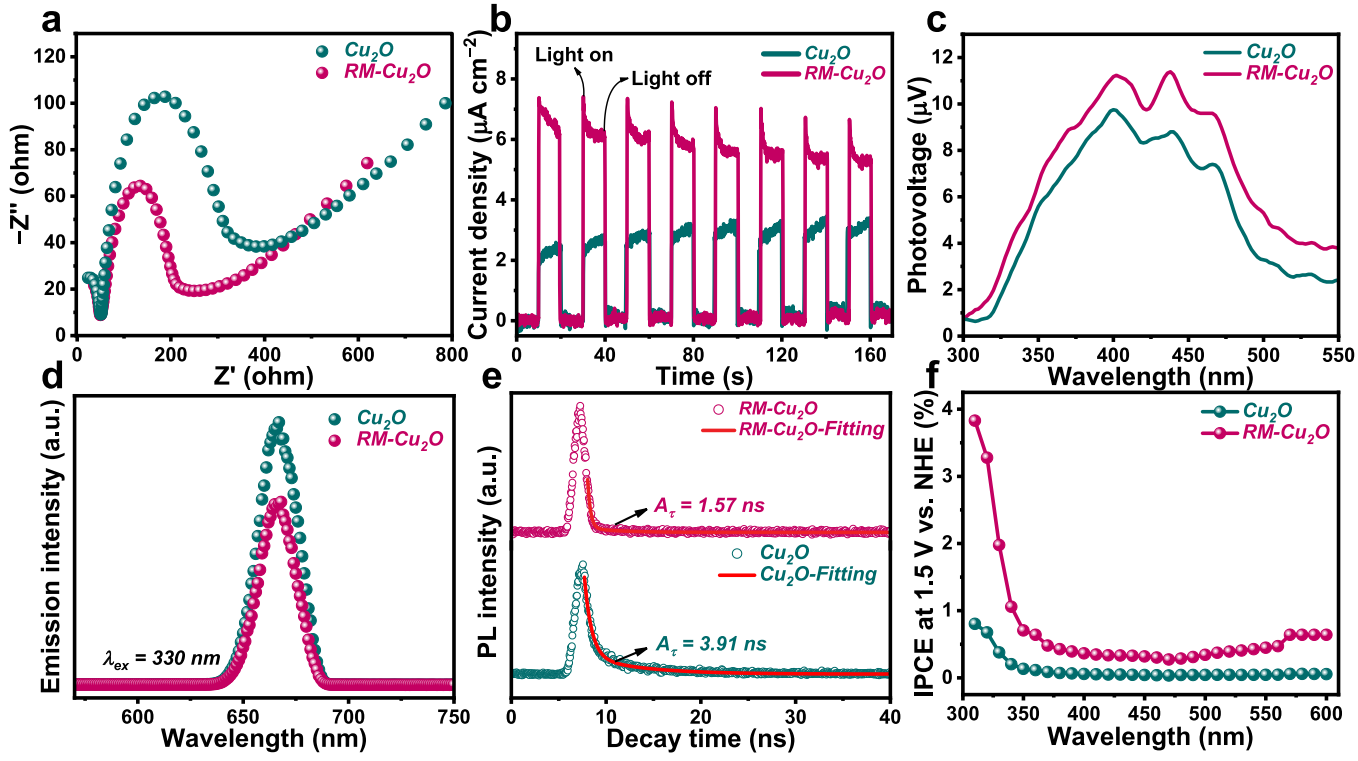

Fig. 4. Photoelectrochemical measurements of Cu_2O and RM-Cu_2O: (a) EIS spectra; (b) Transient photocurrent responses; (c) SPV spectra; (d) Steady-state PL spectra; (e) TR-PL spectra; and (f) IPCE measurements.

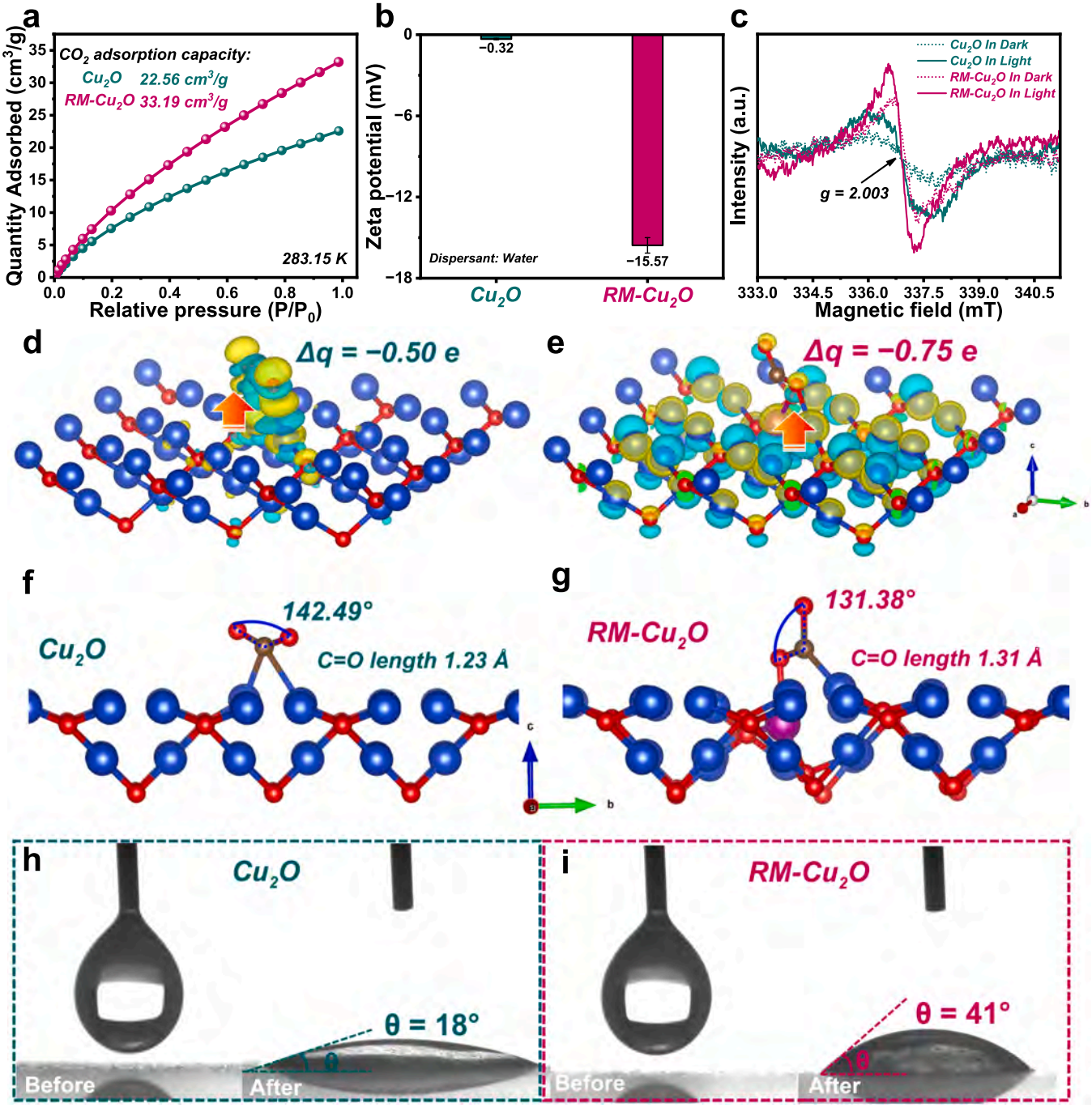

Fig. 5. Surface characterization: (a) CO_2 adsorption isotherm at 1 atm and 283.15 K; (b) Zeta potentials; (c) EPR tests of Cu_2O and RM-Cu_2O; Differential charge densities of (d) Cu_2O-CO_2 and (e) RM-Cu_2O-CO_2; CO_2 adsorption and activation of (f) Cu_2O and (g) RM-Cu_2O; Water contact angles on (h) Cu_2O and (i) RM-Cu_2O.

(22.56 cm^3/g). Hence, more CO_2 molecules can adsorb on the surface of RM-Cu_2O to facilitate PCRR [54]. The surface charge affects the PCRR and the zeta potentials are determined. As shown in Fig. 5b, RM-Cu_2O has a more negative zeta potential, implying more negative charges due to the formation of oxygen vacancies (OVs) during the glucose reduction process [55]. The more negative zeta potential illustrates an electron-rich state in RM-Cu_2O, which is beneficial to the separation of photogenerated carriers and conductivity [56].

Electron paramagnetic resonance (EPR) is performed under dark and light conditions to investigate the OVs. As shown in Fig. 5c, a single Lorentz peak is observed at g = 2.003 from both Cu_2O and RM-Cu_2O, corresponding to free electrons trapped by the OVs. The OVs are formed by the loss of surface oxygen atoms during glucose reduction. RM-Cu_2O shows stronger OV signals under both dark and light conditions compared to the pristine Cu_2O, indicating a larger OV concentration in RM-Cu_2O. The high-concentration OVs bode well for the PCRR [57,58]. The charge density difference of CO_2 on Cu_2O and RM-Cu_2O are calculated. As shown in Figs. 5d and e, the Bader charge of RM-Cu_2O has a more negative value (−0.75 e) than Cu_2O (−0.50 e), indicating that the asymmetric Mn−Cu site provides more electrons for the activation of CO_2 molecules in the PCRR process [59].

The changes in bond length and bond angle of adsorbed CO_2 on the constructed Mn-Cu double sites are studied by DFT calculations (Figs. 5f and g). In the CO_2 adsorption configuration on Cu_2O at a single metal site, the C atom of CO_2 is bonded to the two Cu atoms of Cu_2O with a C−O−C bond angle of 142.49° and C−O bond length of 1.23 Å. In the

adsorption configuration of CO_2 on RM-Cu_2O, the C atoms and O atoms of CO_2 are bonded to Mn and Cu atoms, respectively. As a result, the adsorbed CO_2 on RM-Cu_2O shows a bond length of 1.31 Å and a bond angle of 131.38°. The longer bond and smaller angles are more conducive to the breakage of C═O bonds, thus promoting the activation of CO_2 molecules [60]. Wettability is an important factor affecting the molecular interactions of reactants. As shown in Figs. 5h and i, RM-Cu_2O shows a larger water contact angle (CA = 41°) than Cu_2O (CA = 18°) and better hydrophobic properties, rendering RM-Cu_2O more conducive to enhancing the adsorption and activation of CO_2 molecules in PCRR by repelling water and enriching CO_2 molecules [61,62].

To further explore the charge transfer pathway of RM-Cu_2O in the photocatalytic process, *in situ* irradiation XPS (Fig. S18) is carried out under illumination, as shown in Fig. 6a–c. After illumination, there is no evident shift in Cu 2*p*, while Mn 2*p* shifts toward lower binding energy, revealing that Mn can obtain electrons provided by other elements under illumination [63]. The lattice oxygen spectra shift to higher binding energy, indicating that the photo-generated electrons may be transferred to Mn by the oxygen atom in the PCRR. *In situ* Fourier transform infrared spectroscopy (FTIR) is performed to investigate the

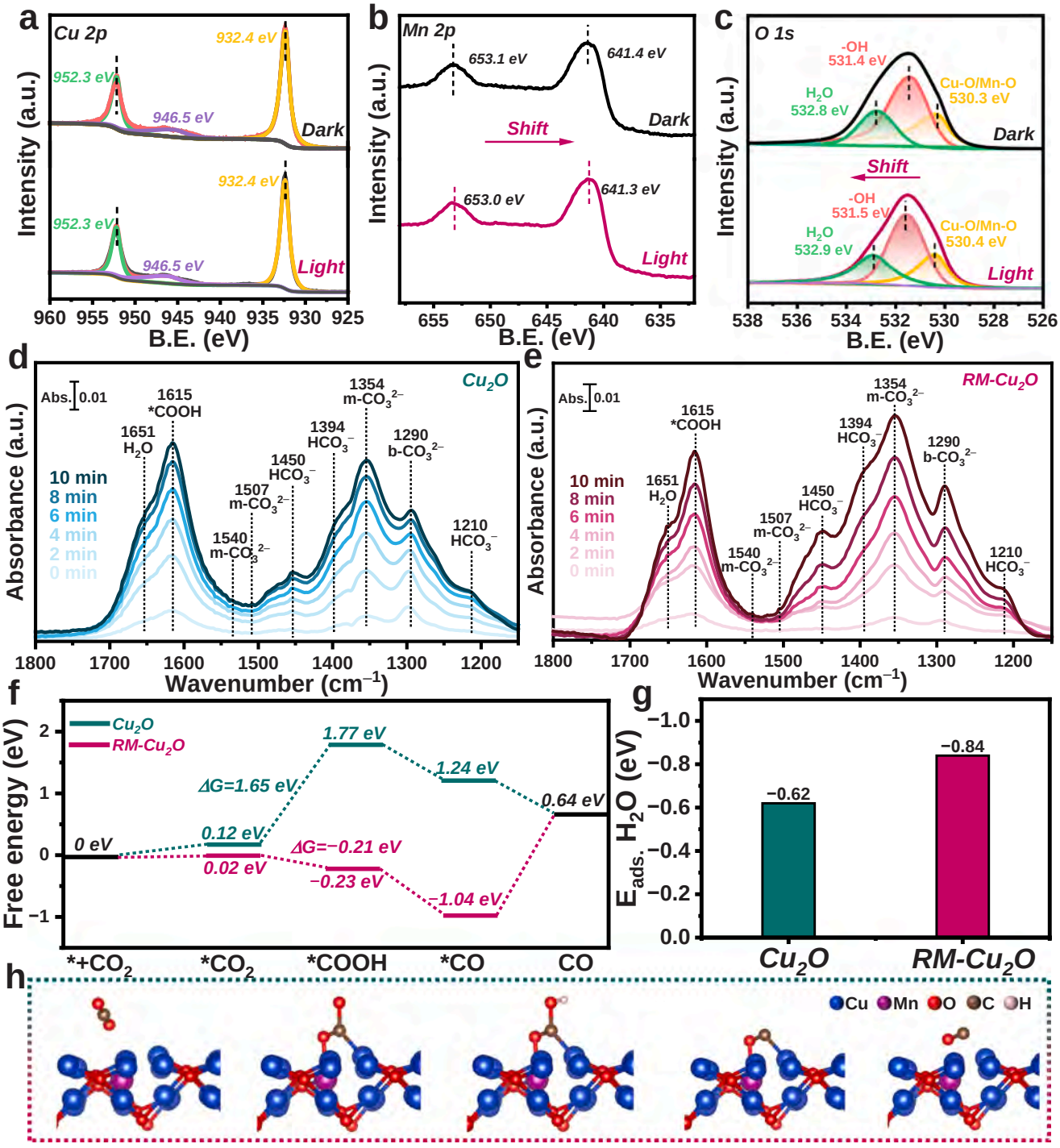

Fig. 6. Exploration of reaction mechanisms: *In situ* irradiation XPS spectra: (a) Cu 2*p*, (b) Mn 2*p*, and (c) O 1 *s*; *In situ* FTIR spectra of (d) Cu_2O and (e) RM-Cu_2O catalyst; (f) Free energy diagrams of CO_2 reduction to CO catalyzed by Cu_2O and RM-Cu_2O; (g) Adsorption energies of H_2O molecules on Cu_2O and RM-Cu_2O; (g) Adsorption configurations of the key intermediates in PCRR.

interactions of surface species and catalysts under the conditions of the simulation experiments, as shown in Figs. 6d and e. Only a few absorption peaks associated with carbonate species are observed under dark conditions, but there are plenty of intermediates for CO_2 hydrogenation under upon full-spectrum illumination, such as HCO_3^- (1210, 1394, and 1450 cm^{-1}), bidentate carbonate species (b-CO_3^{2-}, 1290 cm^{-1}), monodentate carbonate (m-CO_3^{2-}, 1354, 1507, and 1540 cm^{-1}), C═O stretching of *COOH species (1615 cm^{-1}), and adsorbed water (1651 cm^{-1}) stretching vibration [42,64,65]. These intermediates and illumination time show a positive correlation, implying continuous CO_2 activation in the PCRR [42]. *COOH, a key intermediate in CO_2-to-CO conversion, shows a strong increasing trend, demonstrating the formation of a dominant CO product [66]. The concentration of m-CO_3^{2-} in RM-Cu_2O increases significantly compared to Cu_2O. The high-concentration m-CO_3^{2-} species, as another important intermediate in CO_2-to-CO conversion, is not only beneficial to protonation but also renders CO_2 adsorption more stable [67].

The Gibbs free energy (Fig. 6f and Tables S2 and S3) are calculated for the critical steps in the PCRR. The conversion of *CO_2 to *COOH by Cu_2O is the rate-determining step of PCRR ($\Delta G = 1.65$ eV). After constructing asymmetric Mn−Cu sites, ΔG of the *COOH step for RM-Cu_2O is −0.21 eV, suggesting that *COOH intermediates are generated spontaneously [68]. The asymmetric Mn−Cu sites reduce the energy barrier for the conversion of CO_2 to CO with the adsorbed COOH intermediate [69]. The adsorption energies of H_2O (Fig. 6g) are calculated, and H_2O adsorption on RM-Cu_2O is stronger. The above results indicate that the asymmetric Mn−Cu sites accelerate CO_2 activation and reduce the energy barrier of *COOH formation for enhanced PCRR. The process of adsorption and activation of CO_2 on the surface of RM-Cu_2O is shown in Fig. 6h.

4. Conclusions

The Mn-doped Cu_2O (RM-Cu_2O) catalyst with asymmetric Mn−Cu sites is synthesized by a glucose reduction method using Mn-pre-saturated HKUST-1 as the precursor. The catalyst delivers excellent photocatalytic syngas production performance in a pure water system. Owing to the construction of symmetric Mn−Cu sites, RM-Cu_2O shows optimized photogenerated charge transport as well as CO_2 adsorption and activation, resulting in enhanced PCRR activity. *In situ* irradiation XPS and FTIR, together with DFT calculations, reveal the dynamic process in PCRR. The results reveal a promising solution for the post-treatment of the spent MOF-based adsorbents and their application in photocatalysis.

CRediT authorship contribution statement

Ganghua Zhou: Methodology, Conceptualization, Investigation, Data curation, Writing – original draft. **Yun Chen:** Supervision, Resources, Methodology, Writing – review & editing, Funding acquisition, Conceptualization. **Gaoran Chen:** Investigation. **Hangmin Xu:** Investigation. **Weiqin Yin:** Investigation. **Bin Wang:** Investigation. **Xingwang Zhu**: Supervision, Resources, Methodology, Writing – review & editing, Funding acquisition, Conceptualization. **Xin Ning**: Supervision, Resources, Methodology, Writing – review & editing, Funding acquisition, Conceptualization. **Paul K. Chu**: Supervision, Resources, Methodology, Writing – review & editing, Funding acquisition, Conceptualization. **Xiaozhi Wang:** Supervision, Resources, Methodology, Writing – review & editing, Funding acquisition, Conceptualization. **Hui Xu**: Supervision, Methodology.

Declaration of Competing Interest

The authors declare that they have no known competing financial interests or personal relationships that could have appeared to influence the work reported in this paper.

Data availability

Data will be made available on request.

Acknowledgments

This work was jointly supported by the National Natural Science Foundation of China (22308300, 22108106), 333 Project in Jiangsu Province (BRA2020300), Key University Science Research Project of Jiangsu Province (21KJB610003), Natural Science Foundation of Jiangsu Province (BK20220598), Key Laboratory of Electrochemical Energy Storage and Energy Conversion of Hainan Province (KFKT2022001), City University of Hong Kong Donation Research Grants (DON-RMG 9229021; 9220061), and Post-graduate Research & Practice Innovation Program of Jiangsu Province (KYCX23_3554). The authors thank Prof. Ziran Chen from Sichuan Vocational and Technical College generously for providing us with access to the Vienna ab initio simulation package.

Appendix A. Supporting information

Supplementary data associated with this article can be found in the online version at doi:10.1016/j.apcatb.2024.124617.

References

[1] F. Jiao, J. Li, X. Pan, J. Xiao, H. Li, H. Ma, M. Wei, Y. Pan, Z. Zhou, M. Li, S. Miao, J. Li, Y. Zhu, D. Xiao, T. He, J. Yang, F. Qi, Q. Fu, X. Bao, Selective conversion of syngas to light olefins, Science 351 (2016) 1065–1068.
[2] X. Pan, F. Jiao, D. Miao, X. Bao, Oxide-zeolite-based composite catalyst concept that enables syngas chemistry beyond fischer-tropsch synthesis, Chem. Rev. 121 (2021) 6588–6609.
[3] F. Arcudi, L. Ethordevic, N. Schweitzer, S.I. Stupp, E.A. Weiss, Selective visible-light photocatalysis of acetylene to ethylene using a cobalt molecular catalyst and water as a proton source, Nat. Chem. 14 (2022) 1007–1012.
[4] G. Zhou, H. Xu, H. Song, J. Yi, X. Wang, Z. Chen, X. Zhu, Photocatalysis toward microplastics conversion: a critical review, ACS Catal. 14 (2024) 8694–8719.
[5] J. Albero, Y. Peng, H. García, Photocatalytic CO_2 reduction to C2+ products, ACS Catal. 10 (2020) 5734–5749.
[6] Y. Chen, Z. Lai, X. Zhang, Z. Fan, Q. He, C. Tan, H. Zhang, Phase engineering of nanomaterials, Nat. Rev. Chem. 4 (2020) 243–256.
[7] X. Li, W. Wang, F. Dong, Z. Zhang, L. Han, X. Luo, J. Huang, Z. Feng, Z. Chen, G. Jia, T. Zhang, Recent advances in noncontact external-field-assisted photocatalysis: from fundamentals to applications, ACS Catal. 11 (2021) 4739–4769.
[8] H. Huang, H. Song, J. Kou, C. Lu, J. Ye, Atomic-level insights into surface engineering of semiconductors for photocatalytic CO_2 reduction, J. Energy Chem. 67 (2022) 309–341.
[9] Z. Chen, J. Zhang, S. Deng, M. Hou, X. Zhang, Z. Jiang, N.-C. Lai, Morphology-controlled synthesis of Cu_2O encapsulated phase change materials: photothermal conversion and storage performance in visible light regime, Chem. Eng. J. 454 (2023) 140089.
[10] C.Y. Toe, Z. Zheng, H. Wu, J. Scott, R. Amal, Y.H. Ng, Photocorrosion of cuprous oxide in hydrogen production: rationalising self-oxidation or self-reduction, Angew. Chem. Int. Ed. 57 (2018) 13613–13617.
[11] Y. Wang, Q. Wang, J. Wu, X. Zhao, Y. Xiong, F. Luo, Y. Lei, Asymmetric atomic sites make different: recent progress in electrocatalytic CO_2 reduction, Nano Energy 103 (2022) 107815.
[12] C. He, Y. Gong, S. Li, J. Wu, Z. Lu, Q. Li, L. Wang, S. Wu, J. Zhang, Single-atom alloys materials for CO_2 and CH_4 catalytic conversion, Adv. Mater. 36 (2024) e2311628.
[13] Y. Ma, Y. Zhang, G. Xie, Z. Huang, L. Peng, C. Yu, X. Xie, S. Qu, N. Zhang, Isolated Cu sites in CdS hollow nanocubes with doping-location-dependent performance for photocatalytic CO_2 reduction, ACS Catal. 14 (2024) 1468–1479.
[14] X. Xiong, Y. Zhao, R. Shi, W. Yin, Y. Zhao, G.I.N. Waterhouse, T. Zhang, Selective photocatalytic CO_2 reduction over Zn-based layered double hydroxides containing tri or tetravalent metals, Sci. Bull. 65 (2020) 987–994.
[15] P. Liu, B. Yang, Z. Xiao, S. Wang, S. Wu, M. Liu, G. Chen, X. Liu, R. Ma, N. Zhang, Engineering d-band states of $(CuGa)_xZn_{1-2x}Ga_2S_4$ material for photocatalytic syngas production, J. Energy Chem. 79 (2023) 365–372.
[16] G. Qian, W. Lyu, X. Zhao, J. Zhou, R. Fang, F. Wang, Y. Li, Efficient photoreduction of diluted CO_2 to tunable syngas by Ni-Co dual sites through d-band center manipulation, Angew. Chem. Int. Ed. 61 (2022) e202210576.
[17] G.T. Park, S.B. Kim, J.I. Yoon, N.Y. Park, M.C. Kim, S.M. Han, D.H. Kim, M.S. Kim, Y.K. Sun, Unraveling the new role of manganese in nano and microstructural engineering of Ni-rich layered cathode for advanced lithium-ion batteries, Adv. Energy Mater. 14 (2024) 2400130.

[18] Y. Zhang, T. Hou, Q. Xu, Q. Wang, Y. Bai, S. Yang, D. Rao, L. Wu, H. Pan, J. Chen, G. Wang, J. Zhu, T. Yao, X. Zheng, Dual-metal sites boosting polarization of nitrogen molecules for efficient nitrogen photofixation, Adv. Sci. 8 (2021) 2400130.
[19] C. Zhou, X. Chen, S. Liu, Y. Han, H. Meng, Q. Jiang, S. Zhao, F. Wei, J. Sun, T. Tan, R. Zhang, Superdurable bifunctional oxygen electrocatalyst for high-performance zinc-air batteries, J. Am. Chem. Soc. 144 (2022) 2694–2704.
[20] A. Zhang, Y. Liang, H. Li, X. Zhao, Y. Chen, B. Zhang, W. Zhu, J. Zeng, Harmonizing the electronic structures of the adsorbate and catalysts for efficient CO_2 reduction, Nano Lett. 19 (2019) 6547–6553.
[21] Z. Song, Y. Liu, Y. Zhong, Q. Guo, J. Zeng, Z. Geng, Efficient electroreduction of nitrate into ammonia at ultralow concentrations via an enrichment effect, Adv. Mater. 34 (2022) e2204306.
[22] M. Zhang, J. Wang, H. Xue, J. Zhang, S. Peng, X. Han, Y. Deng, W. Hu, Acceptor-doping accelerated charge separation in Cu_2O photocathode for photoelectrochemical water splitting: theoretical and experimental studies, Angew. Chem. Int. Ed. 59 (2020) 18463–18467.
[23] X. Zhu, Y. Cao, Y. Song, J. Yang, X. She, Z. Mo, Y. She, Q. Yu, X. Zhu, J. Yuan, H. Li, H. Xu, Unique dual-sites boosting overall CO_2 photoconversion by hierarchical electron harvesters, Small 17 (2021) e2103796.
[24] X. Zhang, S. Zhang, Y. Yang, L. Wang, Z. Mu, H. Zhu, X. Zhu, H. Xing, H. Xia, B. Huang, J. Li, S. Guo, E. Wang, A general method for transition metal single atoms anchored on honeycomb-like nitrogen-doped carbon nanosheets, Adv. Mater. 32 (2020) e1906905.
[25] T. Cui, L. Ma, S. Wang, C. Ye, X. Liang, Z. Zhang, G. Meng, L. Zheng, H.S. Hu, J. Zhang, H. Duan, D. Wang, Y. Li, Atomically dispersed Pt-N_3C_1 sites enabling efficient and selective electrocatalytic C-C bond cleavage in lignin models under ambient conditions, J. Am. Chem. Soc. 143 (2021) 9429–9439.
[26] Y. Zhou, Q. Gu, K. Yin, Y. Li, L. Tao, H. Tan, Y. Yang, S. Guo, Engineering e_g orbital occupancy of Pt with Au alloying enables reversible Li-O_2 batteries, Angew. Chem. Int. Ed. 61 (2022) e202201416.
[27] H. Zhao, L. Zhu, J. Yin, J. Jin, X. Du, L. Tan, Y. Peng, P. Xi, C.H. Yan, Stabilizing lattice oxygen through Mn doping in $NiCo_2O_4$-d spinel electrocatalysts for efficient and durable acid oxygen evolution, Angew. Chem. Int. Ed. 63 (2024) e202402171.
[28] T. Zhang, Z. Sun, S. Li, B. Wang, Y. Liu, R. Zhang, Z. Zhao, Regulating electron configuration of single Cu sites via unsaturated N,O-coordination for selective oxidation of benzene, Nat. Commun. 13 (2022) 6996.
[29] M. Behera, G. Giri, Green synthesis and characterization of cuprous oxide nanoparticles in presence of a bio-surfactant, Mater. Sci. 32 (2014) 702–708.
[30] X. Yu, J. Zhang, J. Zhang, J. Niu, J. Zhao, Y. Wei, B. Yao, Photocatalytic degradation of ciprofloxacin using Zn-doped Cu_2O particles: analysis of degradation pathways and intermediates, Chem. Eng. J. 374 (2019) 316–327.
[31] S.K. Shinde, D.P. Dubal, G.S. Ghodake, P. Gomez-Romero, S. Kim, V.J. Fulari, Influence of Mn incorporation on the supercapacitive properties of hybrid CuO/Cu$(OH)_2$ electrodes, RSC Adv. 5 (2015) 30478–30484.
[32] H. Chen, X. Dong, J. Shi, J. Zhao, Z. Hua, J. Gao, M. Ruan, D. Yan, Templated synthesis of hierarchically porous manganese oxide with a crystalline nanorod framework and its high electrochemical performance, J. Mater. Chem. 17 (2007) 855.
[33] Z. Landolsi, I. Ben Assaker, A.Y.A. Alzahrani, S.M.A.S. Keshk, R. Chtourou, Thin-film electrodeposition of Fe_2O_3/MnO_2 on TiO_2 as an anode for high energy density hybrid supercapacitor, J. Mater. Sci. Mater. Electron. 33 (2022) 24857–24868.
[34] J.A. Lett, S.F. Alshahateet, I. Fatimah, R.P. Sivasankaran, A.K. Sibhatu, M.-V. Le, S. Sagadevan, Hydrothermal synthesis and photocatalytic activity of Mn_3O_4 nanoparticles, Top. Catal. 66 (2022) 126–138.
[35] M.S. Alam, D. Gorman-Lewis, N. Chen, S. Safari, K. Baek, K.O. Konhauser, D. S. Alessi, Mechanisms of the removal of U(VI) from aqueous solution using biochar: a combined spectroscopic and modeling approach, Environ. Sci. Technol. 52 (2018) 13057–13067.
[36] X. Wang, L. Lu, B. Wang, Z. Xu, Z. Xin, S. Yan, Z. Geng, Z. Zou, Frustrated lewis pairs accelerating CO_2 reduction on oxyhydroxide photocatalysts with surface lattice hydroxyls as a solid-state proton donor, Adv. Funct. Mater. 28 (2018) 1804191.
[37] T. Wei, Y.-N. Zhu, X. An, L.-M. Liu, X. Cao, H. Liu, J. Qu, Defect modulation of Z-Scheme TiO_2/Cu_2O photocatalysts for durable water splitting, ACS Catal. 9 (2019) 8346–8354.
[38] X. Zhong, Y. Sun, X. Chen, G. Zhuang, X. Li, J.-G. Wang, Mo doping induced more active sites in urchin-like $W_{18}O_{49}$ nanostructure with remarkably enhanced performance for hydrogen evolution reaction, Adv. Funct. Mater. 26 (2016) 5778–5786.
[39] S. Qiao, Y. Chen, Y. Tang, J. Yuan, J. Shen, D. Zhang, Y. Du, Z. Li, D. Yuan, H. Tang, C. Liu, Oxygen vacancy–rich Cu_2O@Cu with a hydrophobic microenvironment for highly selective C-C coupling to generate C_2H_4, Chem. Eng. J. 454 (2023) 140321.
[40] Q. Zhu, K. Zhu, M. Cai, Y. Zhang, Z. Shao, M. Jiang, X. Wang, Z. Geng, X. Wu, M. Li, K. Huang, S. Feng, Electron transfer in Cu/Cu_2O generated by disproportionation promoting efficient CO_2 photoreduction, Nano Res. 15 (2022) 7099–7106.
[41] Y. Wang, J. Hu, T. Ge, F. Chen, Y. Lu, R. Chen, H. Zhang, B. Ye, S. Wang, Y. Zhang, T. Ma, H. Huang, Gradient cationic vacancies enabling inner-to-outer tandem homojunctions: strong local internal electric field and reformed basic sites boosting CO_2 photoreduction, Adv. Mater. 35 (2023) e2302538.
[42] X. Li, L. Li, G. Chen, X. Chu, X. Liu, C. Naisa, D. Pohl, M. Loffler, X. Feng, Accessing parity-forbidden d-d transitions for photocatalytic CO_2 reduction driven by infrared light, Nat. Commun. 14 (2023) 4034.
[43] B. Wang, H. Chen, W. Zhang, H. Liu, Z. Zheng, F. Huang, J. Liu, G. Liu, X. Yan, Y. X. Weng, H. Li, Y. She, P.K. Chu, J. Xia, Semimetallic bismuthene with edge-rich dangling bonds: broad-spectrum-driven and edge-confined electron enhancement boosting CO_2 hydrogenation reduction, Adv. Mater. 36 (2024) e2312676.
[44] G. Liu, F. Zheng, J. Li, G. Zeng, Y. Ye, D.M. Larson, J. Yano, E.J. Crumlin, J. W. Ager, L.-w. Wang, F.M. Toma, Investigation and mitigation of degradation mechanisms in Cu_2O photoelectrodes for CO_2 reduction to ethylene, Nat. Energy 6 (2021) 1124–1132.
[45] Z. Tang, W. He, Y. Wang, Y. Wei, X. Yu, J. Xiong, X. Wang, X. Zhang, Z. Zhao, J. Liu, Ternary heterojunction in rGO-coated Ag/Cu_2O catalysts for boosting selective photocatalytic CO_2 reduction into CH_4, Appl. Catal. B Environ. 311 (2022) 121371.
[46] X. Wang, J. Chen, Q. Li, L. Li, Z. Zhuang, F.F. Chen, Y. Yu, Light-driven syngas production over defective $ZnIn_2S_4$ nanosheets, Chem. Eur. J. 27 (2021) 3786–3792.
[47] Y. Shi, G. Zhan, H. Li, X. Wang, X. Liu, L. Shi, K. Wei, C. Ling, Z. Li, H. Wang, C. Mao, X. Liu, L. Zhang, Simultaneous manipulation of bulk excitons and surface defects for ultrastable and highly selective CO_2 photoreduction, Adv. Mater. 33 (2021) 2100143.
[48] Y. Zhang, C. Pan, G. Bian, J. Xu, Y. Dong, Y. Zhang, Y. Lou, W. Liu, Y. Zhu, H_2O_2 generation from O_2 and H_2O on a near-infrared absorbing porphyrin supramolecular photocatalyst, Nat. Energy 8 (2023) 361–371.
[49] X. Feng, R. Zheng, C. Gao, W. Wei, J. Peng, R. Wang, S. Yang, W. Zou, X. Wu, Y. Ji, H. Chen, Unlocking bimetallic active sites via a desalination strategy for photocatalytic reduction of atmospheric carbon dioxide, Nat. Commun. 13 (2022) 2146.
[50] X. She, X. Zhu, J. Yang, Y. Song, Y. She, D. Liu, J. Wu, Q. Yu, H. Li, Z. Liu, P. M. Ajayan, H. Xu, Grain-boundary surface terminations incorporating oxygen vacancies for selectively boosting CO_2 photoreduction activity, Nano Energy 84 (2021) 105869.
[51] P.M. Ismail, S. Ali, S. Ali, J. Li, M. Liu, D. Yan, F. Raziq, F. Wahid, G. Li, S. Yuan, X. Wu, J. Yi, J.S. Chen, Q. Wang, L. Zhong, Y. Yang, P. Xia, L. Qiao, Photoelectron "bridge" in van der Waals heterojunction for enhanced photocatalytic CO_2 conversion under visible light, Adv. Mater. 35 (2023) e2303047.
[52] B. Sun, C. Huang, C. Yang, D. Ke, Y. Liu, Q. Lu, X. Liu, X. Xiong, Y. Chen, Q. Jiang, J. Hu, T. Zhou, Atomic interfacial charge and energy transfer paths at MoS_2/Pd bonded defect-rich BiOCl interfaces for efficient photocatalysis, Appl. Catal. B Environ. 345 (2024) 123720.
[53] Y. Li, Y. Li, Y. Yin, D. Xia, H. Ding, C. Ding, J. Wu, Y. Yan, Y. Liu, N. Chen, P. K. Wong, A. Lu, Facile synthesis of highly efficient ZnO/$ZnFe_2O_4$ photocatalyst using earth-abundant sphalerite and its visible light photocatalytic activity, Appl. Catal. B Environ. 226 (2018) 324–336.
[54] C. Jia, B. Wan, W. Liu, L. Qi, X. Liu, X. Han, A. Gao, J. Liu, Microenvironment modulation of ultrathin bronze-phase TiO_2 nanosheets for highly selective photocatalytic CO_2 reduction in water, Adv. Funct. Mater. 34 (2023) 2311663.
[55] J. Di, C. Chen, C. Zhu, M. Ji, J. Xia, C. Yan, W. Hao, S. Li, H. Li, Z. Liu, Bismuth vacancy mediated single unit cell Bi_2WO_6 nanosheets for boosting photocatalytic oxygen evolution, Appl. Catal. B Environ. 238 (2018) 119–125.
[56] L. Du, Q. Tian, X. Zheng, W. Guo, W. Liu, Y. Zhou, F. Shi, Q. Xu, Supercritical CO_2-tailored 2D oxygen-doped amorphous carbon nitride for enhanced photocatalytic activity, Energy Environ. Mater. 5 (2021) 912–917.
[57] S. Yang, X. Guo, X. Li, T. Wu, L. Zou, Z. He, Q. Xu, J. Zheng, L. Chen, Q. Wang, Z. J. Xu, Enhancing photocatalytic CO_2 conversion through oxygen-vacancy-mediated topological phase transition, Angew. Chem. Int. Ed. 63 (2024) e202317957.
[58] B. Wang, W. Zhang, G. Liu, H. Chen, Y.X. Weng, H. Li, P.K. Chu, J. Xia, Excited electron-rich $Bi^{(3-x)+}$ sites: a quantum well-like structure for highly promoted selective photocatalytic CO_2 reduction performance, Adv. Funct. Mater. 32 (2022) 2202885.
[59] Y. Mao, M. Zhang, S. Si, G. Zhai, X. Bao, K. Song, L. Zheng, Y. Liu, Z. Wang, Z. Zheng, P. Wang, Y. Dai, H. Cheng, B. Huang, Electronic structure manipulation via site-selective atomically dispersed Ni for efficient photocatalytic CO_2 reduction, ACS Catal. 13 (2023) 8362–8371.
[60] B. Zhou, P. Ou, N. Pant, S. Cheng, S. Vanka, S. Chu, R.T. Rashid, G. Botton, J. Song, Z. Mi, Highly efficient binary copper-iron catalyst for photoelectrochemical carbon dioxide reduction toward methane, PNAS 117 (2020) 1330–1338.
[61] W. Ge, Y. Chen, Y. Fan, Y. Zhu, H. Liu, L. Song, Z. Liu, C. Lian, H. Jiang, C. Li, Dynamically formed surfactant assembly at the electrified electrode–electrolyte interface boosting CO_2 electroreduction, J. Am. Chem. Soc. 144 (2022) 6613–6622.
[62] Q. Huang, C. Chu, Q. Li, Q. Liu, X. Liu, J. Sun, B.-J. Ni, S. Mao, Three-phase interface construction on hydrophobic carbonaceous catalysts for highly active and selective photocatalytic CO_2 conversion, ACS Catal. 13 (2023) 11232–11243.
[63] H. Ren, F. Qi, A. Labidi, J. Zhao, H. Wang, Y. Xin, J. Luo, C. Wang, Chemically bonded carbon quantum dots/Bi_2WO_6 S-scheme heterojunction for boosted photocatalytic antibiotic degradation: interfacial engineering and mechanism insight, Appl. Catal. B Environ. 330 (2023) 122587.
[64] J. Liang, H. Zhang, Q. Song, Z. Liu, J. Xia, B. Yan, X. Meng, Z. Jiang, X.W.D. Lou, C. S. Lee, Modulating charge separation of oxygen-doped boron nitride with isolated Co atoms for enhancing CO_2-to-CO photoreduction, Adv. Mater. 36 (2024) e2303287.
[65] Y. Chai, Y. Kong, M. Lin, W. Lin, J. Shen, J. Long, R. Yuan, W. Dai, X. Wang, Z. Zhang, Metal to non-metal sites of metallic sulfides switching products from CO to CH_4 for photocatalytic CO_2 reduction, Nat. Commun. 14 (2023) 6168.
[66] K. Zhu, Q. Zhu, M. Jiang, Y. Zhang, Z. Shao, Z. Geng, X. Wang, H. Zeng, X. Wu, W. Zhang, K. Huang, S. Feng, Modulating Ti t_{2g} orbital occupancy in a Cu/TiO_2 composite for selective photocatalytic CO_2 reduction to CO, Angew. Chem. Int. Ed. 61 (2022) e202207600.

[67] Y. Zhang, X. Zhi, J.R. Harmer, H. Xu, K. Davey, J. Ran, S.Z. Qiao, Facet-specific active surface regulation of Bi_xMO_y (M=Mo, V, W) nanosheets for boosted photocatalytic CO_2 reduction, Angew. Chem. Int. Ed. 61 (2022) e202212355.
[68] P. Yang, Z.J. Zhao, X. Chang, R. Mu, S. Zha, G. Zhang, J. Gong, The functionality of surface hydroxy groups on the selectivity and activity of carbon dioxide reduction over cuprous oxide in aqueous solutions, Angew. Chem. Int. Ed. 57 (2018) 7724–7728.
[69] X. Xiong, C. Mao, Z. Yang, Q. Zhang, G.I.N. Waterhouse, L. Gu, T. Zhang, Photocatalytic CO_2 reduction to CO over Ni single atoms supported on defect-rich zirconia, Adv. Energy Mater. 10 (2020) 2002928.

Supplementary Information

Enhanced CO_2 Photoreduction in Pure Water Systems by Surface-Reconstructed Asymmetric Mn−Cu Sites

Ganghua Zhou[a], Yun Chen[a,*], Gaoran Chen[a], Hangmin Xu[a], Weiqin Yin[a], Bin Wang[b], Xingwang Zhu[a,*], Xin Ning[a,], Paul K. Chu[b,*], Xiaozhi Wang[a,c,d,**], Hui Xu[e]

[a] School of Mechanical Engineering, College of Environmental Science and Engineering, Institute of Technology for Carbon Neutralization, Yangzhou University, Yangzhou, Jiangsu 225009, P. R. China

[b] Department of Physics, Department of Materials Science and Engineering, and Department of Biomedical Engineering City University of Hong Kong Tat Chee Avenue, Kowloon, Hong Kong, China

[c] Joint International Research Laboratory of Agriculture and Agri-Product Safety of Ministry of Education of China, Yangzhou University, Yangzhou, Jiangsu 225009, P. R. China

[d] Jiangsu Collaborative Innovation Center for Solid Organic Waste Resource Utilization, Nanjing, Jiangsu 210095, P. R. China

[e] School of the Environment and Safety Engineering, Institute for Energy Research, Jiangsu University, Zhenjiang 212013, PR China

* Email addresses: cy@zxw.ac.cn (Y. Chen); zxw@yzu.edu.cn (X. Zhu); paul.chu@cityu.edu.hk (P. Chu); xzwang@yzu.edu.cn (X. Wang)

Characterization

The crystal structures of the catalysts were characterized by a Bruker D8 ADVANCE diffractometer with monochromatized Cu K_α radiation (λ = 1.5418 Å). The Fourier transform infrared spectroscopy (FTIR) spectra were recorded by averaging 32 scans with a resolution of 4 cm^{-1} on the Nicolet IS5 spectrophotometer (Thermo Fisher Scientific, America). The morphologies of the materials were observed by scanning electron microscopy (SEM, GeminiSEM 300, Carl Zeiss, Germany), transmission electron microscopy (TEM, Philips, Tecnai 12, Netherlands), high-resolution transmission electron microscopy (HR-TEM, FEI Tecnai G2 F20 S-TWIN, USA), and spherical aberration-corrected high-resolution transmission electron microscopy (AC HRTEM, Titan G2, FEI). X-ray photoelectron spectroscopy (XPS) was carried out on the Nexsa G2 instrument (Thermo Fisher Scientific, USA) to analyze the chemical states. The XPS fine spectra were analyzed by the AVANTAGE software and calibrated with reference to the C 1*s* peak at 284.8 eV. The Brunauer-Emmett-Teller (BET) surface areas were calculated based on the N_2 adsorption-desorption method on the Micromeritics ASAP2460 (Micromeritics Instrument Co., Norcross, GA). The diffuse reflectance spectra (DRS) were obtained on a UV-Vis-NIR spectrometer (Agilent, Cary5000), and a steady fluorescence spectrophotometer (PL, Hitachi F7000) was utilized to evaluate the charge recombination rates. The transient fluorescence lifetimes of the catalysts were determined on the transient state fluorescence spectrometer (Edinburgh Instruments, FLS980). The steady-state surface photovoltages (SPV) and incident photon-to-current efficiency (IPCE) of the catalysts were measured on the PL-

SPV/IPCE1000 (PerfectLight, China). The oxygen vacancies were detected on the A300-10/12 Bruker EPR spectrometer, and the JCY2 contact angle instrument was used to measure the static water contact angles. The Mn concentration was determined by inductively-coupled plasma mass spectrometry (ICP-MS, iCAPTM QC, and *in situ* FTIR was performed on the Thermo Scientific Nicolet iS50 spectrometer.

Photo/electrochemical measurements

The photo/electrochemical measurements, including electrochemical impedance spectroscopy and transient photocurrent detection, were performed on the DH7000C electrochemical workstation (Jiangsu Donghua Instrument Co., Ltd. China) with a three-electrode cell, in which Ag/AgCl and Pt wire were the counter electrode and reference electrode, respectively. The working electrodes were prepared by the drip-coating method. Typically, the catalyst (10 mg) was dispersed ultrasonically in a mixture containing 0.45 mL of H_2O, 0.45 mL of ethanol, and, 0.1 mL of Nafion. Afterward, the slurry was dropped onto an ITO glass substrate and dried at 60 ℃. All the photoelectrochemical measurements were performed using a 300 W Xenon lamp as the light source and 0.2 M Na_2SO_4 as the electrolyte.

***In situ* irradiated XPS**

In situ irradiated XPS was carried out on the Nexsa G2 spectrometer (Thermo Fisher Scientific, USA) equipped with a monochromatic Al source with a beam spot of 400 μm. The transmitted optical fiber light was used to study the dynamic changes in the chemical environment of the sample under light irradiation in *situ*. The pass energy of the XPS survey spectrum was 100 eV, with a step size of 1.0 eV. The pass energy of the fine spectrum was 50 eV, with a step size of 0.05 eV. All the XPS spectra were referenced to the C 1*s* peak at 284.8 eV.

Theoretical Calculations

The computation utilized the plane-wave density functional theory (DFT) approach implemented in the Vienna ab initio simulation package (VASP). The projector-augmented waves method was employed to characterize the interactions between electrons and ions. To sample the Brillouin zone integrals, a Monkhorst-Pack K-point grid with dimensions of 3×3×1 was adopted. The convergence criteria for both the geometric optimization and electronic structure calculations were set up to ensure a total energy change of < 0.05 eV/Å and ion relaxation energy $\leq 1.0\times10^{-4}$. In determining the work function (φ), a vacuum layer 10 Å thick was applied, and the DFT-D3 method was used to correct the van der Waals (vdW) interactions.

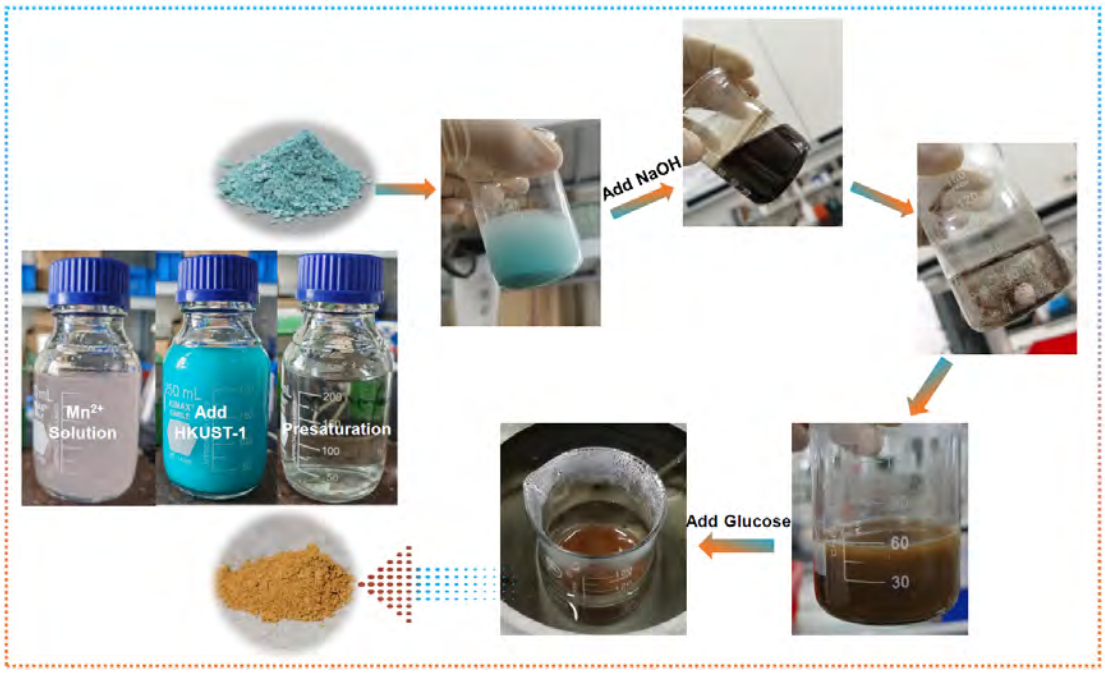

Fig. S1. Photographs taken during the various states in the synthesis of the RM-Cu_2O catalyst.

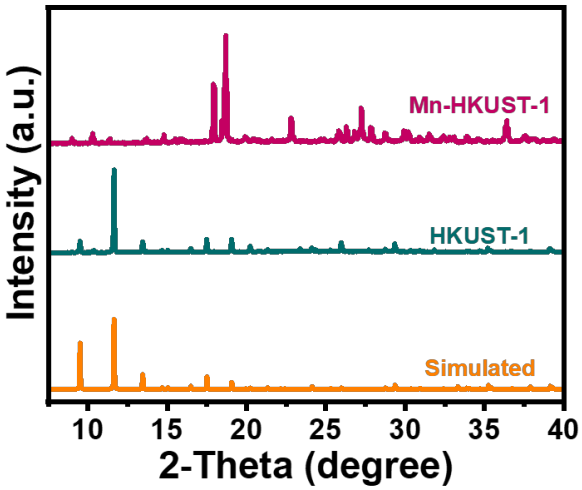

Fig. S2. XRD patterns of HKUST-1 and Mn-HKUST-1.

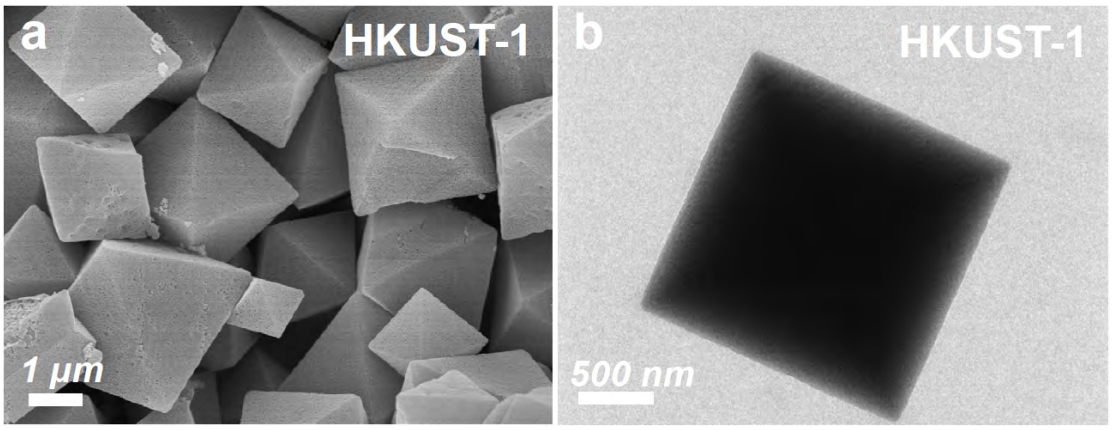

Fig. S3. (a) SEM and (b) TEM images of HKUST-1.

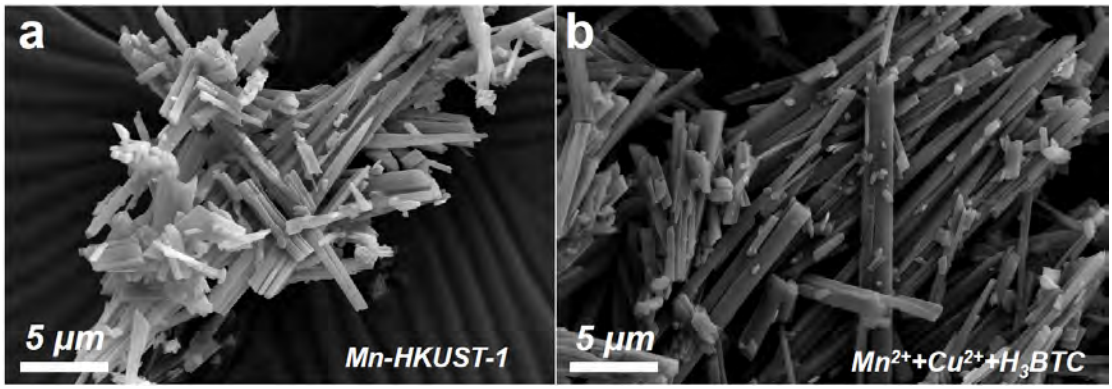

Fig. S4. SEM image of (a) Mn-HKUST-1 and (b) TEM image of Mn^{2+}+Cu^{2+}+H_3BTC.

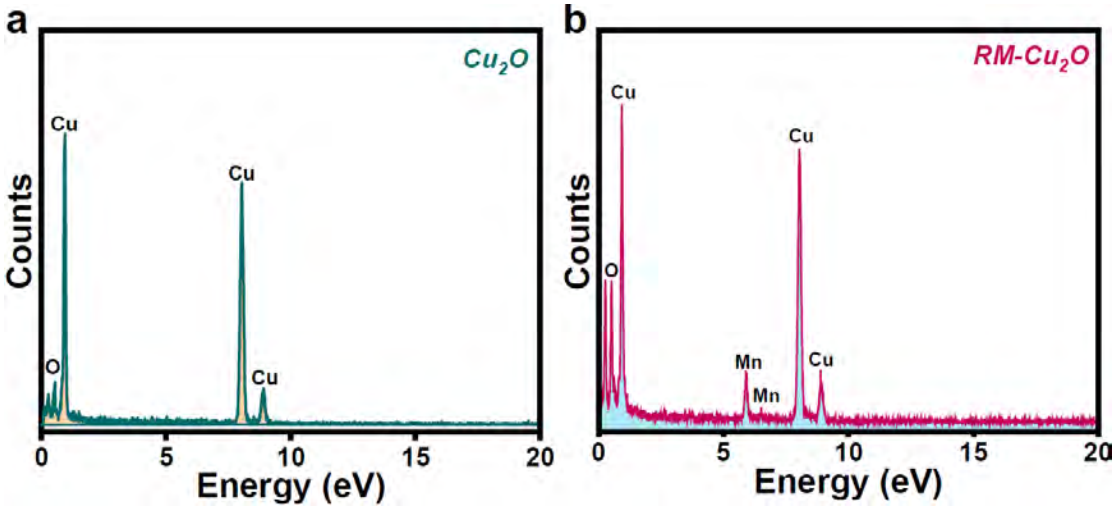

Fig. S5. EDX spectra of (a) Cu_2O and (b) RM-Cu_2O.

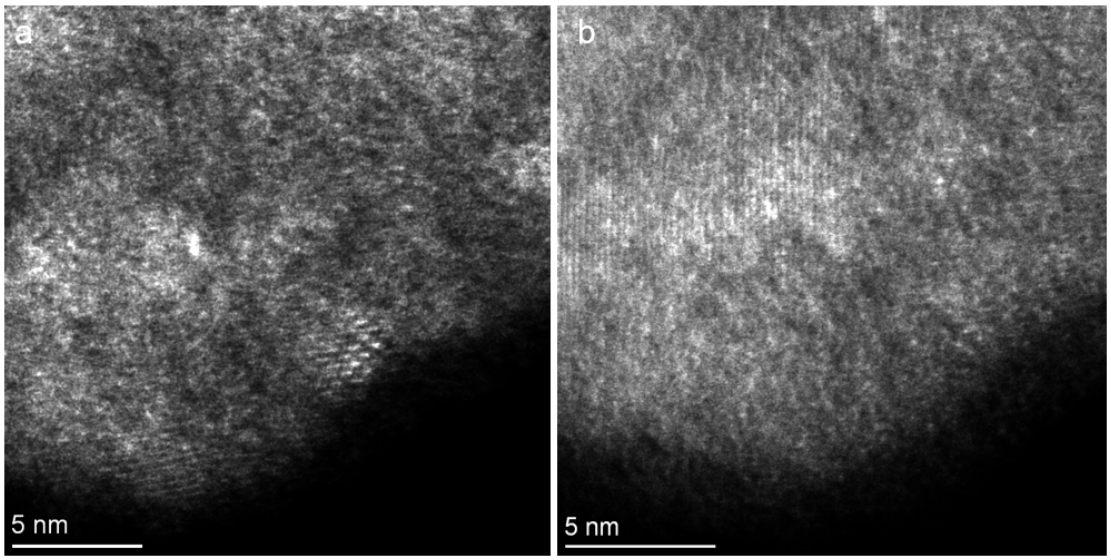

Fig. S6. AC STEM images of RM-Cu_2O catalyst.

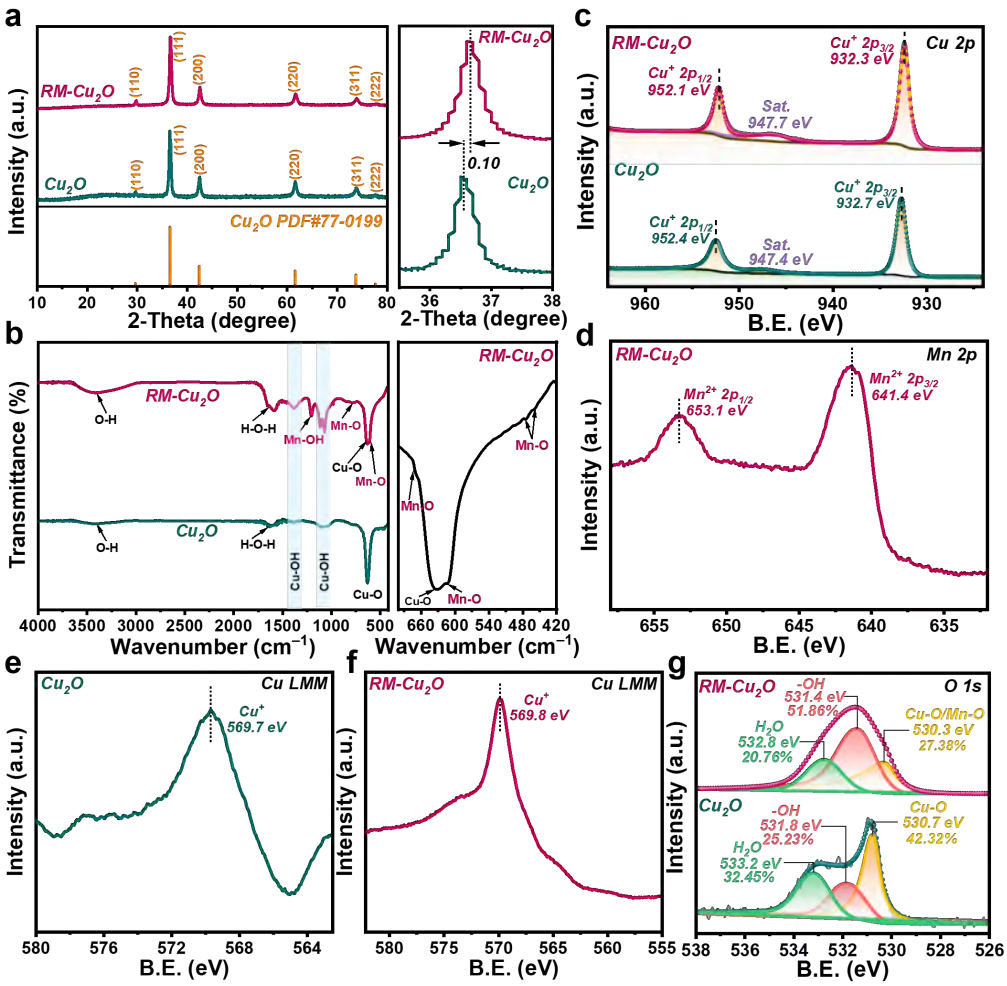

Fig. S7. Surface structure and chemical states: (a) XRD patterns; (b) FTIR spectra; XPS spectra of (c) Cu 2*p* and (d) Mn 2*p*; Auger Cu LMM spectra of (e) Cu_2O and (f) RM-Cu_2O; (g) XPS O 1*s* spectra.

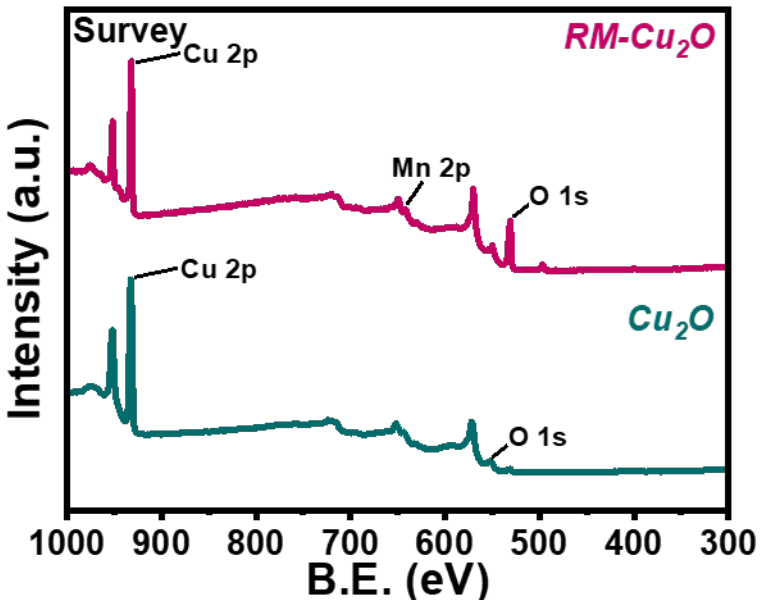

Fig. S8. XPS survey spectra of the as-prepared samples.

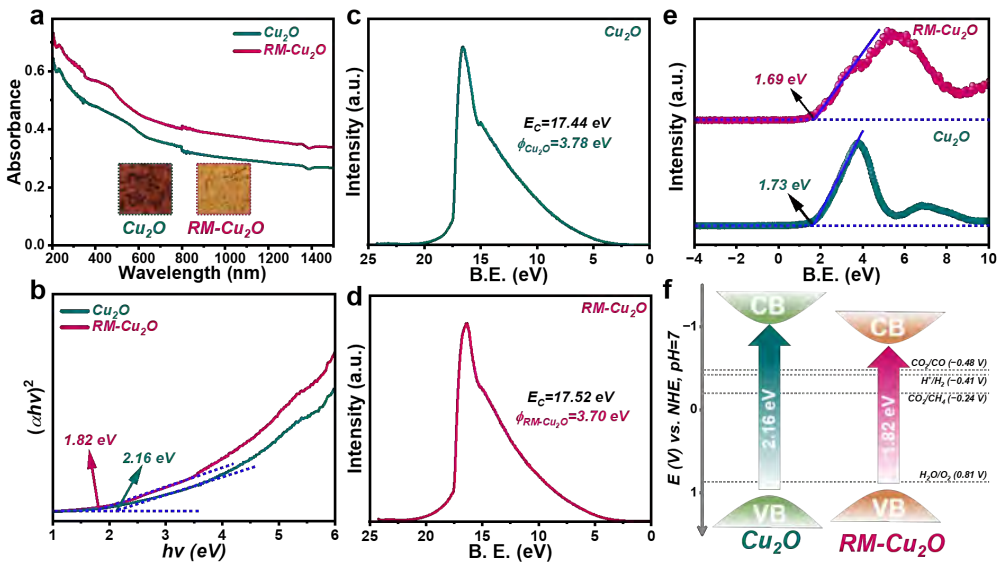

Fig. S9. Band structures: (a) DRS spectra and (b) Tauc plots of Cu_2O and RM-Cu_2O; UPS spectra of (c) Cu_2O and (d) RM-Cu_2O; (e) XPS-VB spectra; (f) Schematic illustrations of the electronic band structures of Cu_2O and RM-Cu_2O.

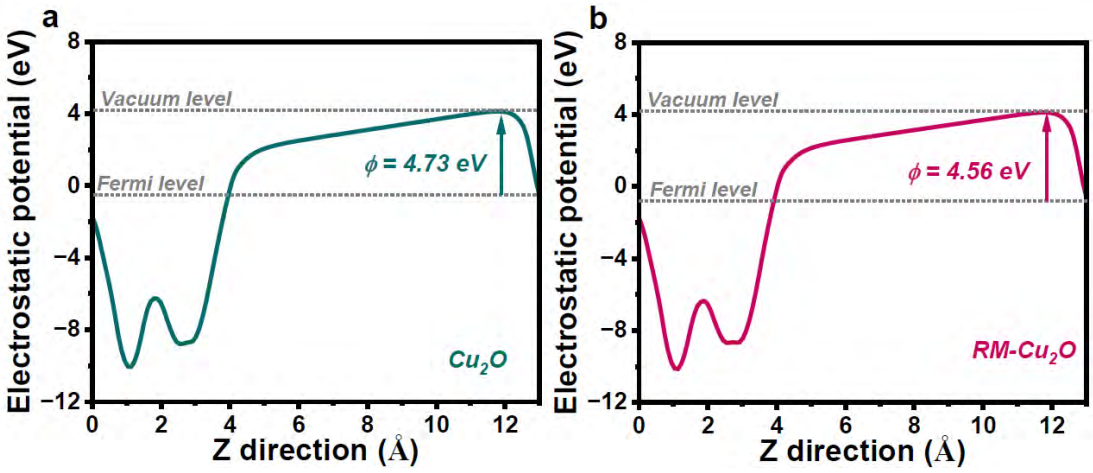

Fig. S10. Calculated work functions of Cu_2O and RM-Cu_2O.

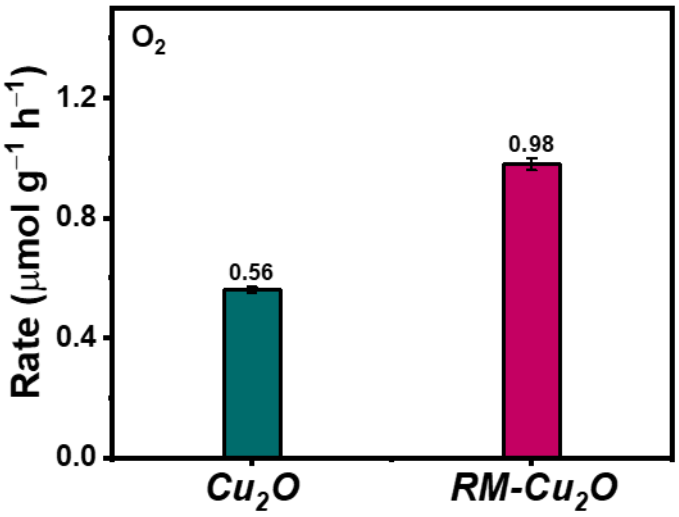

Fig. S11. The O_2 yields of as-synthesized photocatalysts.

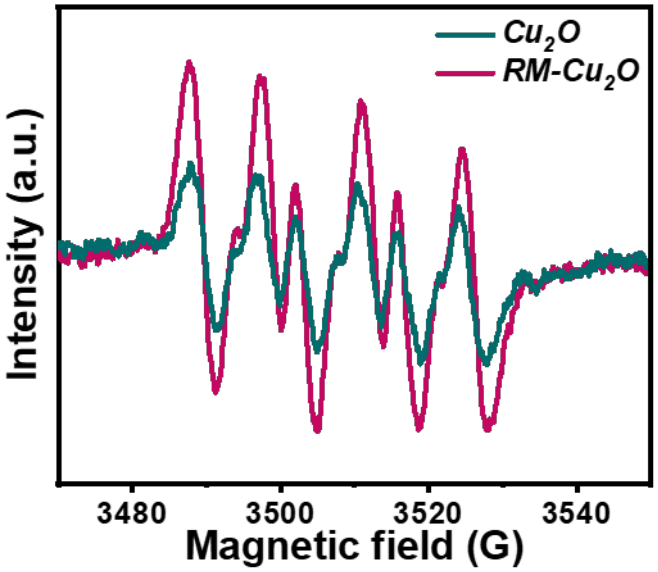

Fig. S12. EPR tests for superoxide radical.

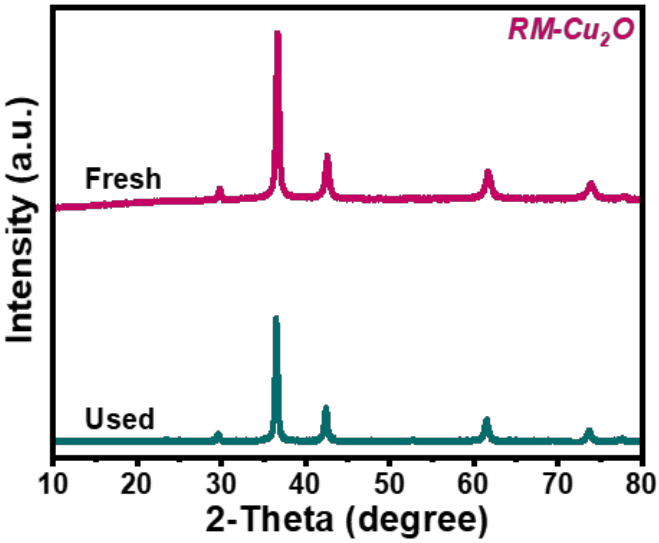

Fig. S13. XRD patterns of RM-Cu_2O before and after PCRR.

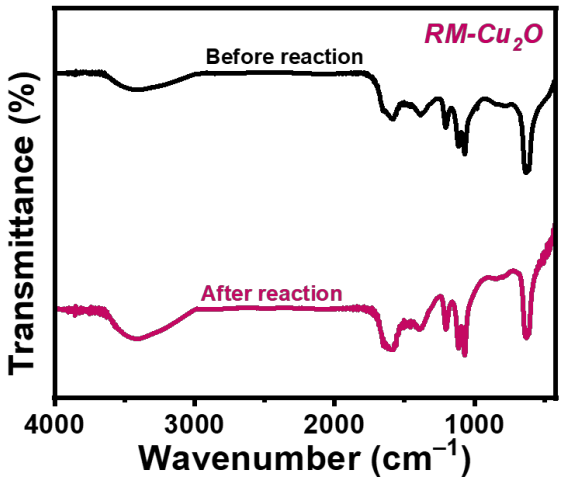

Fig. S14. FTIR spectra of RM-Cu_2O before and after PCRR.

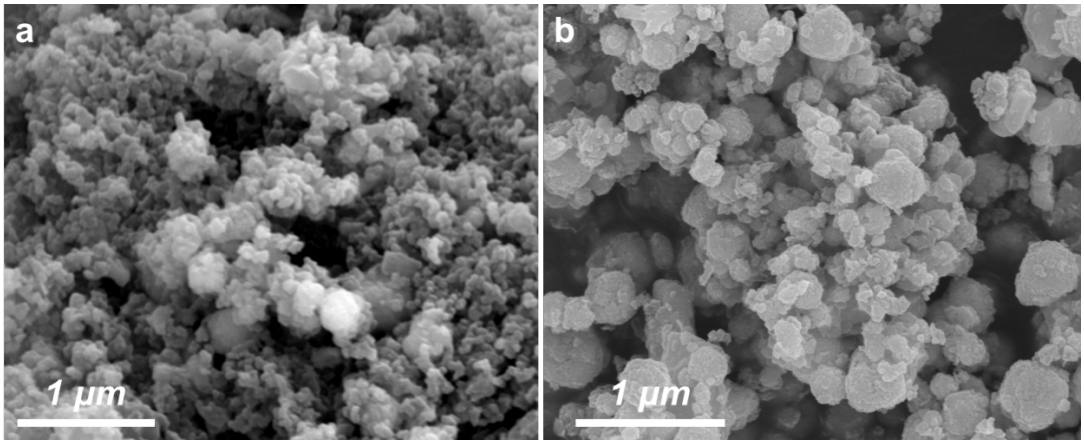

Fig. S15. SEM images of RM-Cu_2O (a) before and (b) after PCRR.

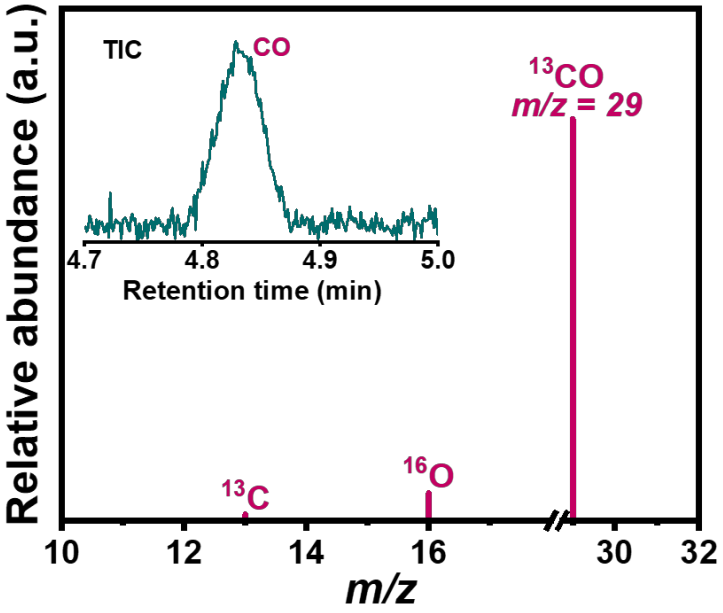

Fig. S16. Isotope labeling experiments for CO.

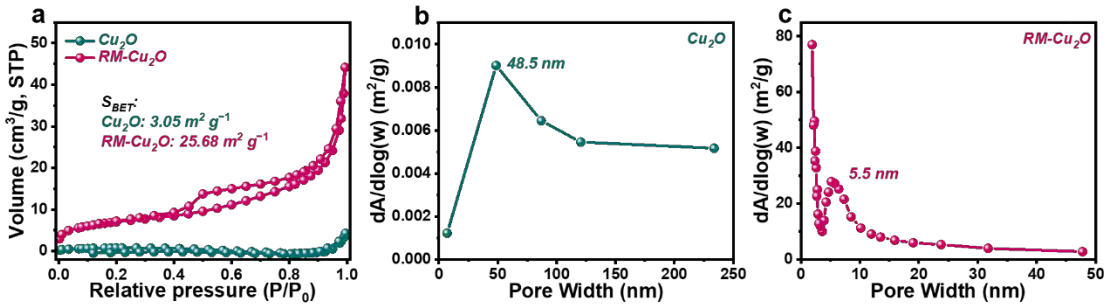

Fig. S17. (a) N_2 adsorption-desorption isotherms of the catalysts; Pore size distributions of (b) Cu_2O and (c) RM-Cu_2O.

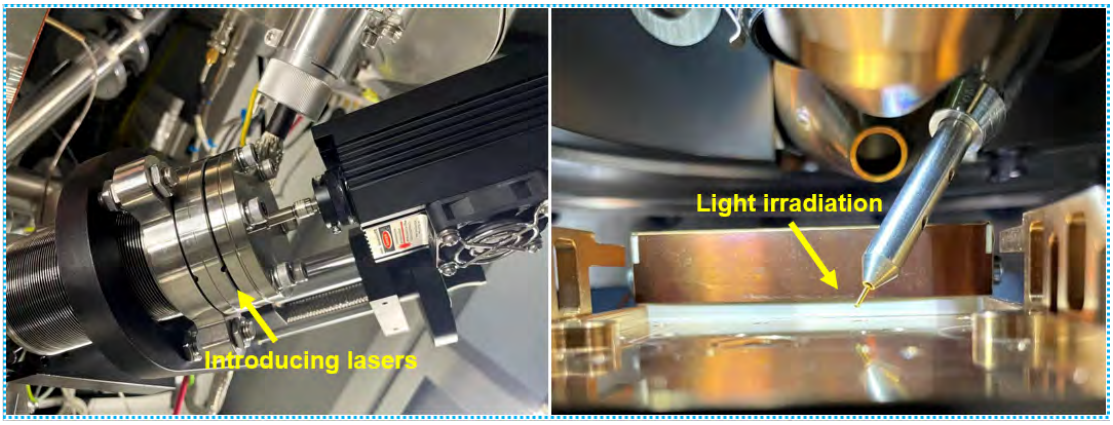

Fig. S18. Pictures of the setup for *in situ* irradiated XPS.

Table S1. Lifetimes of Cu_2O and RM-Cu_2O catalysts.

Photocatalysts	τ_1 **(ns)**	A_1	**Rel. %**	τ_2 **(ns)**	A_2	**Rel. %**	χ^2	**Average lifetime (A_τ) (ns)**
Cu_2O	0.76	377.57	37.73	5.81	81.66	62.27	1.27	3.91
RM-Cu_2O	0.30	219.00	55.42	3.14	17.03	44.58	1.16	1.57

Table S2. Energies of the Cu_2O surface and reaction intermediates.

Cu_2O	**Slab (*)**	***CO_2**	***COOH**	***CO**	**CO**
E/eV	−230.63	−252.99	−257.42	−247.13	−242.11
ΔE/eV	0.00	0.62	−2.71	−2.20	−5.02
ΔG/eV	0.00	1.09	−2.28	−2.70	−4.53
G/eV	0.00	1.09	−1.19	−3.89	0.64

Table S3. Energies of the RM-Cu_2O surface and reaction intermediates.

RM-Cu_2O	**Slab (*)**	***CO_2**	***COOH**	***CO**	**CO**
E/eV	−236.18	−259.56	−264.73	−253.25	−250.68
ΔE/eV	0.00	−0.40	−3.45	−1.01	−2.57
ΔG/eV	0.00	0.07	−3.02	−1.51	−2.08
G/eV	0.00	0.07	−2.95	−1.44	0.64